Computers and Structures 291 (2024) 107209

Contents lists available at ScienceDirect

Computers and Structures

journal homepage: www.elsevier.com/locate/compstruc

Lamination-based efficient treatment of weak discontinuities for non-conforming finite element meshes

Jędrzej Dobrzański, Kajetan Wojtacki, Stanisław Stupkiewicz *

Institute of Fundamental Technological Research, Polish Academy of Sciences, Pawińskiego 5B, 02-106 Warsaw, Poland

ARTICLE INFO

Keywords:
Finite element method
Interface
Weak discontinuity
Laminate
Homogenization
Elasticity
Plasticity

ABSTRACT

When modelling discontinuities (interfaces) using the finite element method, the standard approach is to use a conforming finite-element mesh in which the mesh matches the interfaces. However, this natural approach can prove cumbersome if the geometry is complex, in particular in 3D. In this work, we develop an efficient technique for a non-conforming finite-element treatment of weak discontinuities by using laminated microstructures. The approach is inspired by the so-called composite voxel technique that has been developed for FFT-based spectral solvers in computational homogenization. The idea behind the method is rather simple. Each finite element that is cut by an interface is treated as a simple laminate with the volume fraction of the phases and the lamination orientation determined in terms of the actual geometrical arrangement of the interface within the element. The approach is illustrated by several computational examples relevant to the micromechanics of heterogeneous materials. Elastic and elastic-plastic materials at small and finite strain are considered in the examples. The performance of the proposed method is compared to two alternative, simple methods showing that the new approach is in most cases superior to them while maintaining the simplicity.

1. Introduction

Solving partial differential equations on complex geometries plays a dominant role in many problems of interest in computational solid mechanics. Analytical solutions that consider possible geometrical heterogeneities are not available in most cases. Computational approaches are thus indispensable, the finite element method (FEM) being the most general, most powerful and most popular computational tool for numerical simulations in various areas of engineering.

Historically, FEM relies on geometry-dependent computational grids (body-fitted or conforming meshing). This is a natural and preferred approach, as it is characterized by optimal accuracy. However, due to the complexity of investigated geometries, especially internal heterogeneities, a fine conforming discretisation can be quite hard to use. One reason is the limited computational cost that can be afforded. Although algorithms for finite element meshing in 2D are quite efficient and well-established, the mesh generation for 3D problems still remains a rather cumbersome and time-consuming task. This problem is particularly pronounced when discretising geometries that contain discontinuities or objects (details) with diverse characteristic lengths. Secondly, some additional manual input is often needed or use of specialized mesh generation software. Thirdly, for 3D models, especially large-scale ones, unstructured meshes, which are necessarily needed to represent complex geometries, may lead to additional difficulties associated with the assembly and solution of the respective finite-element equations. And finally, even if the previous obstacles can be somehow overcome, additional effort may be needed during post-processing. Overall, mesh generation may become the most time-consuming process in the pre-processing step of numerical modelling, and dealing with conforming meshes for complex geometries may significantly increase the computational expense.

A possible approach to evade the mesh generation problem is to use a non-conforming mesh. In general, the respective methods use a structured mesh or a simple unstructured mesh generated in the domain defined by the external boundary of the modelled geometry. Generating such a mesh is then a straightforward process. However, the internal details of the geometry must somehow be treated, and several approaches have been developed for that purpose, as discussed below.

The focus of this work is on *weak discontinuities*, i.e., on the situation in which the primal variable (e.g., the displacement field) is continuous at the interface and discontinuous are its derivatives and related quantities (e.g., strains and stresses) when the material properties (e.g.,

* Corresponding author.
E-mail addresses: jdobrz@ippt.pan.pl (J. Dobrzański), kajetan.wojtacki@gmail.com (K. Wojtacki), sstupkie@ippt.pan.pl (S. Stupkiewicz).

https://doi.org/10.1016/j.compstruc.2023.107209
Received 29 March 2023; Accepted 25 October 2023
Available online 11 November 2023

elastic moduli) suffer discontinuity at the interface. This is in contrast to strong discontinuities, such as cracks, when the primal variable may be discontinuous at the interface (of possibly unknown and evolving shape). Actually, several methods have been primarily developed for strong discontinuities and have then been adapted to weak discontinuities.

This is, for instance, the case of the extended finite element method (X-FEM) initially developed for modelling crack propagation independent of the underlying finite-element mesh [1,2], see also two methods that are closely related to X-FEM, namely CutFEM [3] and phantom node method (PNM) [4], and are sometimes considered just versions of X-FEM. It has been subsequently shown that X-FEM can be successfully used also for modelling complex internal geometries (weak discontinuities) of the geometry independent of the finite-element mesh [5–7]. With increasing popularity of the isogeometric analysis (IGA) [8], the X-FEM approach has been also combined with IGA [9,10], including XIGA for weak discontinuities and multimaterial problems [11,12].

In X-FEM, the inner surfaces (e.g., material interfaces, cracks) are defined implicitly using level set functions [13]. Enrichment functions are then employed to modify the finite-element approximation of the displacement field such that the discontinuity is represented on a non-matching mesh. As a result, the optimal convergence rate can be achieved. The beneficial features of X-FEM come at the cost that additional global degrees of freedom are introduced (those associated with the enrichment shape functions). Moreover, integration must be performed accurately on the elements cut by an interface and, for this purpose, the elements are triangulated such that the subdomains match the interfaces. This becomes even more complex when more than one interface passes through an element, which is not so improbable, for instance, in the case of small inclusions or multi-material problems. Overall, implementation of X-FEM is not straightforward, particularly in 3D, and cannot be performed solely at the element level.

Additional deformation modes, in a sense similar to the enrichment functions of X-FEM, are also introduced in the immersed interface FEM (IIFEM) [14,15] and in the augmented finite element method (AFEM) [16,17]. The difference is that, unlike in X-FEM, the enrichment functions are not continuous at the inter-element boundaries, which implies that the optimal convergence rate cannot be achieved. To improve convergence, the inter-element compatibility is enforced in a version of IIFEM [18], which then bears some similarity to X-FEM. In the incompatible case, the additional degrees of freedom associated with the additional deformation modes can be condensed at the element level, hence no additional global degrees of freedom are introduced.

Common to the approaches discussed above is the “small cut-cell” problem that may appear when a small part of the element is cut by an interface. This may lead to a large condition number of the algebraic system to be solved and may deteriorate numerical stability of the resulting algorithms, thus additional stabilization techniques are needed.

A different approach is adopted in the shifted interface method (SIM) [19,20] in which the interface is shifted to a nearby inter-element boundary. At the same time, to compensate for the error introduced by shifting the interface, the interface jump (compatibility) conditions are applied at the surrogate interface in a modified form resulting from the Taylor expansion of the original jump conditions. As a result, the optimal convergence rate can be achieved [19].

In this work, we develop a simple method for improved treatment of weak discontinuities in non-conforming FEM discretization. The inspiration comes from recent developments in the FFT-based methods in computational homogenization. In this class of approaches [21], a periodic unit cell is discretized into a regular array of voxels, hence complex-shaped interfaces cannot be represented exactly. In order to increase the accuracy of FFT-based homogenization, the idea of *composite voxels* has been introduced in [22], see also [23] for a related approach in the context of FEM, and was the first attempt to use a homogenization technique to prescribe effective mechanical properties to the voxel that contains an interface between two phases. This idea was further developed by considering the composite voxel to be represented by a *laminated microstructure* and characterized by the corresponding effective properties [24,25]. It has been shown that these laminate voxels significantly improve the accuracy of the method as compared to the composite voxels employing simple Voigt and Reuss bounds [25]. Lamination-based composite voxels have also been found effective in reducing spurious oscillations [24], the so-called Gibbs oscillations that occur at the locations of high contrast in material properties and are characteristic for FFT-based schemes. Further related developments in the context of FFT-based homogenization include the extension to inelastic problems [26,27] and to the finite-strain framework [28,29].

In this work, the idea of laminate-based composite voxels is applied in the context of the finite element method. In short, each element that is cut by an interface is treated as a laminate composed of the two phases with the volume fraction and lamination orientation determined by the actual geometry of the interface within the element, see Section 3. The method, which we call the laminated element technique (LET), does not introduce any additional global degrees of freedom and can be implemented solely at the element level. Direct application of LET and simple laminates is limited to the case of maximum one interface contained within each element, thus, for instance, triple junctions are not allowed. Possible generalizations are briefly commented at the end of Section 3. The performance of the method is examined through several numerical experiments, see Section 4.

As illustrated by the numerical examples, in terms of accuracy, the proposed method cannot compete, and is not aimed to compete, with more sophisticated methods, such as X-FEM, which can achieve the optimal convergence rate typical for conforming-mesh FEM. However, the beneficial features of LET, as compared to X-FEM, are its simplicity and the ease of implementation. At the same time, it delivers an improved accuracy, as compared to two simple non-conforming mesh approaches examined as a reference. Compared to those simple approaches and also to the standard conforming-mesh approach, LET is associated with additional data storage and with extra computational cost related to the more complex constitutive description of laminates. However, this only concerns the laminated elements (those cut by interfaces) which constitute only a small fraction of all elements, and this fraction decreases with increasing mesh density.

2. Preliminaries

2.1. Compatibility conditions at a bonded interface

Consider a body occupying, in the reference configuration, domain Ω that is divided into two subdomains Ω_1 and Ω_2 ($\Omega = \Omega_1 \cup \Omega_2$, $\Omega_1 \cap \Omega_2 = \emptyset$) with homogeneous material properties within subdomains Ω_1 and Ω_2. The interface separating Ω_1 and Ω_2 is assumed to be smooth and is denoted by Σ with $\boldsymbol{N}$ denoting the unit normal outward to Ω_1.

Deformation of the body is described by the deformation mapping $\boldsymbol{\varphi}$ such that $\boldsymbol{x} = \boldsymbol{\varphi}(\boldsymbol{X}) = \boldsymbol{X} + \boldsymbol{u}(\boldsymbol{X})$ where $\boldsymbol{X}$ and $\boldsymbol{x}$ denote the position of a material point in the reference and current configuration, respectively, and $\boldsymbol{u}$ is the displacement field. The deformation mapping is assumed to be continuously differentiable in Ω_1 and in Ω_2 and continuous on Σ. The deformation gradient $\boldsymbol{F} = \nabla\boldsymbol{\varphi}$ can thus be defined in Ω_1 and in Ω_2, while continuity of $\boldsymbol{\varphi}$ implies the following *kinematic compatibility condition* on Σ, e.g. [30],

$$\boldsymbol{F}_2 - \boldsymbol{F}_1 = \boldsymbol{c} \otimes \boldsymbol{N}, \tag{1}$$

where $\boldsymbol{F}_1$ and $\boldsymbol{F}_2$ are the two limiting values of the deformation gradient at the interface Σ, $\boldsymbol{c}$ is a vector, ∇ denotes the gradient in the reference configuration, and $\otimes$ denotes the dyadic product. The interface Σ is thus a surface of weak discontinuity at which the displacement is continuous, but the deformation gradient $\boldsymbol{F}$ (and thus also the stress) may suffer discontinuity due to the jump in the material properties at Σ.

The equilibrium equation, $\nabla \cdot \boldsymbol{P}^{\mathrm{T}} = \boldsymbol{0}$ ($P_{ij,j} = 0$), is formulated in Ω_1 and in Ω_2 in terms of the Piola (first Piola–Kirchhoff) stress tensor

$\boldsymbol{P} = J\boldsymbol{\sigma}\boldsymbol{F}^{-\mathrm{T}}$, where $\boldsymbol{\sigma}$ is the Cauchy stress tensor, and $J = \det \boldsymbol{F}$. At the interface, equilibrium requires that the traction vector is continuous,

$$(\boldsymbol{P}_2 - \boldsymbol{P}_1)\boldsymbol{N} = \boldsymbol{0}, \tag{2}$$

which can be written also in the current configuration, $(\boldsymbol{\sigma}_2 - \boldsymbol{\sigma}_1)\boldsymbol{n} = \boldsymbol{0}$, where $\boldsymbol{n}$ is the normal to the interface in the current configuration.

In the small-strain (geometrically linear) framework, the compatibility conditions, Eqs. (1) and (2), take the following form,

$$\boldsymbol{\varepsilon}_2 - \boldsymbol{\varepsilon}_1 = \frac{1}{2}(\boldsymbol{c}\otimes\boldsymbol{n} + \boldsymbol{n}\otimes\boldsymbol{c}), \qquad (\boldsymbol{\sigma}_2 - \boldsymbol{\sigma}_1)\boldsymbol{n} = \boldsymbol{0}, \tag{3}$$

where $\boldsymbol{\varepsilon}$ is the usual infinitesimal strain tensor (the symmetric part of the displacement gradient), and no distinction is made between the current and reference configurations, hence $\boldsymbol{n} = \boldsymbol{N}$.

2.2. Simple laminate

A simple laminate is a microstructure composed of layers of two phases (materials) separated by parallel planar interfaces. Under the usual assumption of separation of scales, strains and stresses are homogeneous within each individual layer and are identical in all layers of the same phase. The microstructure is then fully characterized by the volume fractions of the phases, $\eta_1 = 1 - \eta$ and $\eta_2 = \eta$, where $0 \le \eta \le 1$, and by the interface normal $\boldsymbol{N}$, all referred to the reference configuration.

Since the strains and stresses are piecewise homogeneous, the macroscopic deformation gradient $\bar{\boldsymbol{F}}$ and the macroscopic Piola stress $\bar{\boldsymbol{P}}$ are obtained as simple weighted averages of the respective local quantities,

$$\bar{\boldsymbol{F}} = \{\boldsymbol{F}\} = (1-\eta)\boldsymbol{F}_1 + \eta\boldsymbol{F}_2, \qquad \bar{\boldsymbol{P}} = \{\boldsymbol{P}\} = (1-\eta)\boldsymbol{P}_1 + \eta\boldsymbol{P}_2, \tag{4}$$

where $\{\square\}$ denotes the average over the representative volume element in the reference configuration. Here, $\boldsymbol{F}_i$ and $\boldsymbol{P}_i$ denote the local quantities within the individual phases.

The compatibility conditions, Eqs. (1) and (2), and the averaging rules, Eq. (4), complemented by the local constitutive laws of the phases, are sufficient to determine the macroscopic constitutive law relating the macroscopic quantities, $\bar{\boldsymbol{F}}$ and $\bar{\boldsymbol{P}}$. This is illustrated below for the case of hyperelastic constituents. The general case of elastic-plastic phases is discussed in Appendix A, where the corresponding computational scheme is presented including the structure of the nested iterative-subiterative scheme and its linearization.

A hyperelastic material model is fully defined by specifying the elastic strain energy function. Denoting by $W_i = W_i(\boldsymbol{F}_i)$ the elastic strain energy of phase i, the corresponding Piola stress $\boldsymbol{P}_i$ is obtained as

$$\boldsymbol{P}_i = \frac{\partial W_i(\boldsymbol{F}_i)}{\partial \boldsymbol{F}_i}. \tag{5}$$

While the requirement of objectivity implies that W_i is in fact a function of the right Cauchy–Green tensor $\boldsymbol{C}_i = \boldsymbol{F}_i^{\mathrm{T}}\boldsymbol{F}_i$, it is convenient here to keep the deformation gradient $\boldsymbol{F}_i$ as the argument of W_i. Since the constituent phases are hyperelastic, the laminate is also a hyperelastic material. Its behaviour is thus governed by the corresponding (macroscopic) elastic strain energy function that depends on the macroscopic deformation gradient $\bar{\boldsymbol{F}}$, as discussed below.

Using the kinematic compatibility condition (1) and the averaging rule $(4)_1$, the local deformation gradients $\boldsymbol{F}_i$ can be expressed in terms of the macroscopic deformation gradient $\bar{\boldsymbol{F}}$ and (yet unknown) jump vector $\boldsymbol{c}$,

$$\boldsymbol{F}_1 = \bar{\boldsymbol{F}} - \eta\boldsymbol{c}\otimes\boldsymbol{N}, \qquad \boldsymbol{F}_2 = \bar{\boldsymbol{F}} + (1-\eta)\boldsymbol{c}\otimes\boldsymbol{N}. \tag{6}$$

The macroscopic elastic strain energy $\bar{W} = \{W\}$ is thus also a function of $\bar{\boldsymbol{F}}$ and $\boldsymbol{c}$,

$$\bar{W}(\bar{\boldsymbol{F}}, \boldsymbol{c}) = (1-\eta)W_1(\boldsymbol{F}_1) + \eta W_2(\boldsymbol{F}_2). \tag{7}$$

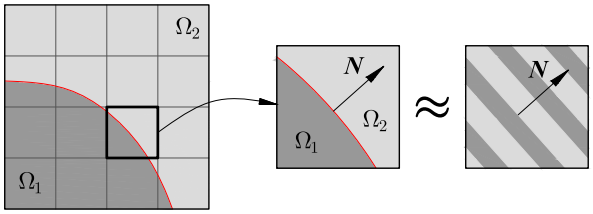

Fig. 1. Laminated element technique (LET): the element that is cut by an interface is treated as a simple laminate with the volume fraction and lamination orientation specified by the actual geometry of the interface within the element. $\boldsymbol{N}$ is the unit normal to the interface.

The unknown vector $\boldsymbol{c}$ can now be determined from the compatibility condition (2). The local deformation gradients $\boldsymbol{F}_i$ specified by Eq. (6) are kinematically admissible since this representation satisfies the kinematic compatibility condition (1) and the averaging rule $(4)_1$ by construction. Accordingly, the local equilibrium of the laminate, expressed by the compatibility condition (2), corresponds to the minimum of the macroscopic elastic strain energy with respect to $\boldsymbol{c}$ (at prescribed $\bar{\boldsymbol{F}}$). Indeed, the condition of stationarity of $\bar{W}$ gives

$$\boldsymbol{0} = \frac{\partial \bar{W}}{\partial \boldsymbol{c}} = (1-\eta)\frac{\partial W_1}{\partial \boldsymbol{F}_1}\frac{\partial \boldsymbol{F}_1}{\partial \boldsymbol{c}} + \eta\frac{\partial W_2}{\partial \boldsymbol{F}_2}\frac{\partial \boldsymbol{F}_2}{\partial \boldsymbol{c}} = \eta(1-\eta)(\boldsymbol{P}_2 - \boldsymbol{P}_1)\boldsymbol{N}, \tag{8}$$

which is equivalent to Eq. (2) in the non-trivial case of $0 < \eta < 1$.

Eq. (2) is a nonlinear equation to be solved for the unknown vector $\boldsymbol{c}$, for instance, using the Newton method. The solution of Eq. (2) depends (implicitly) on $\bar{\boldsymbol{F}}$ so that we have $\boldsymbol{c} = \boldsymbol{c}(\bar{\boldsymbol{F}})$. The macroscopic elastic strain energy can thus be written as a function of $\bar{\boldsymbol{F}}$ only,

$$\bar{W}^*(\bar{\boldsymbol{F}}) = \bar{W}(\bar{\boldsymbol{F}}, \boldsymbol{c}(\bar{\boldsymbol{F}})), \tag{9}$$

such that $\bar{W}^*$ indeed governs the macroscopic response of the laminate,

$$\bar{\boldsymbol{P}} = \frac{\partial \bar{W}^*}{\partial \bar{\boldsymbol{F}}}. \tag{10}$$

To prove Eq. (10), we observe that

$$\begin{aligned}\frac{\partial \bar{W}^*}{\partial \bar{\boldsymbol{F}}} &= \frac{\partial \bar{W}}{\partial \bar{\boldsymbol{F}}} + \frac{\partial \bar{W}}{\partial \boldsymbol{c}}\frac{\partial \boldsymbol{c}}{\partial \bar{\boldsymbol{F}}} = (1-\eta)\frac{\partial W_1}{\partial \boldsymbol{F}_1}\frac{\partial \boldsymbol{F}_1}{\partial \bar{\boldsymbol{F}}} + \eta\frac{\partial W_2}{\partial \boldsymbol{F}_2}\frac{\partial \boldsymbol{F}_2}{\partial \bar{\boldsymbol{F}}} \\ &= (1-\eta)\boldsymbol{P}_1 + \eta\boldsymbol{P}_2 = \bar{\boldsymbol{P}},\end{aligned} \tag{11}$$

where $\partial \bar{W}/\partial \boldsymbol{c} = \boldsymbol{0}$ in view of Eq. (8). Computation of the tangent moduli tensor is not discussed here since it is discussed in Appendix A in a more general setting.

In the case of linear elastic phases, the laminate is also a linear elastic material fully characterized by a fourth-order tensor of overall elastic moduli. Closed-form formulae for the overall moduli can be found in [31].

3. Laminated element technique

The main idea of the laminated element technique (LET) is rather simple: the finite element that is cut by an interface is treated as a simple laminate composed of the two phases involved, see Fig. 1. No treatment is applied to the elements that fully belong to one phase. In each laminated element, the volume fraction of the phases and the lamination orientation are determined according to the actual geometry of the interface within the element, as described in detail below.

In the continuum setting, the geometry is defined by the level-set function ϕ defined over the whole domain Ω,

$$\phi : \Omega \subset \mathbb{R}^n \to \mathbb{R}, \tag{12}$$

such that $\phi < 0$ corresponds to phase 1, $\phi > 0$ corresponds to phase 2, and the interface Σ separating the two phases is represented by the zero level set,

$$\Sigma = \{\boldsymbol{X} \in \Omega \subset \mathbb{R}^n \mid \phi(\boldsymbol{X}) = 0\}, \tag{13}$$

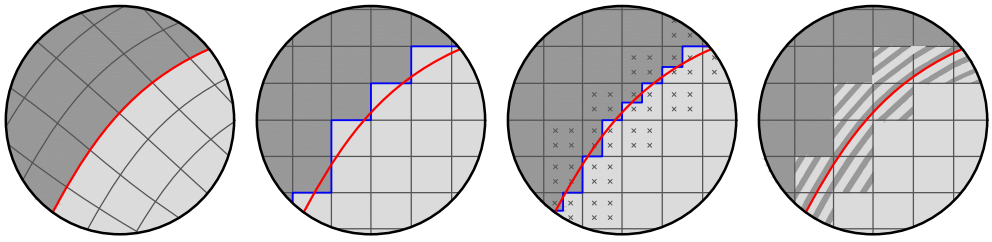

(a) Conforming mesh (b) Element-Level Assignment (c) Gauss-Point-Level Assignment (d) Laminated Element Technique

Fig. 2. Discretization approaches employed in this work: (a) conforming mesh, (b) element-level assignment (ELA), (c) Gauss-point-level assignment (GPLA), and (d) laminated element technique (LET). In ELA (resp. GPLA), the whole element (resp. Gauss point) belongs to a single phase that is determined by the value of the level-set function in the element centre (resp. at the Gauss point).

where $n = 2, 3$ is the space dimension. It is desirable that the level-set function ϕ be smooth and (approximately) proportional to the signed distance from the interface in the nearest neighbourhood of interface (within the range of one finite element) so that the interface is correctly approximated by the zero level set of the finite-element approximation ϕ^h of the level-set function ϕ,

$$\phi^h = \sum_i N_i \phi_i, \tag{14}$$

where N_i are the usual finite-element basis functions and ϕ_i are the nodal values. While the actual level-set function ϕ may be available in some cases, in the following we only use its finite-element approximation ϕ^h. This is a more general approach that is applicable also when the analytical description is not available, for instance, when ϕ^h results from a solution of an independent problem (e.g., microstructure evolution, shape/topology optimization, etc.).

As mentioned in the previous section, a simple laminate is uniquely defined by two quantities, namely the volume fraction η ($\eta_1 = 1-\eta$, $\eta_2 = \eta$) and the unit vector $\boldsymbol{N}$ normal to the interfaces separating the phases (in the reference configuration). These two quantities are determined locally within each laminated element in terms of the level-set function ϕ^h and are assumed constant within each element.

There is some ambiguity concerning determination of the volume fraction. Exact integration of the volume (or area in 2D) is not possible in the general case and is not needed considering the approximation introduced by LET anyway. In this work, we only consider four-node quadrilateral elements in 2D and eight-node hexahedral elements in 3D, and we use the following formula for the volume fraction $\eta^e = \eta_2^e$ in the e-th element,

$$\eta^e = \frac{\sum_{i=1}^{n_\mathrm{n}} \langle \phi_i^e \rangle}{\sum_{i=1}^{n_\mathrm{n}} |\phi_i^e|}, \tag{15}$$

where ϕ_i^e are the nodal values of the level-set function ϕ in the element, n_n is the number of nodes in the element, and $\langle \square \rangle = \frac{1}{2}(\square + |\square|)$ denotes the Macaulay brackets.

In 2D, if the considered element is a rectangle and the interface is a straight line cutting two opposite edges of the rectangle, then formula (15) gives an exact value of the volume fraction. Likewise, in 3D, formula (15) is exact for a planar interface cutting four parallel edges of an element of the shape of a rectangular cuboid. Otherwise, in particular, when the edges are cut differently, formula (15) is approximate. For a non-planar interface, the error decreases with mesh refinement since then the interface effectively tends to be more planar. We have made some efforts to generalize formula (15) to improve its accuracy for elements of arbitrary, non-rectangular shape, for instance, by including the usual quadrature weights at the element nodes, but the simple formula (15) has been found more accurate. Note that, for a planar interface in 2D, the volume fraction can be computed in closed form using the general formula for the area of a polygon in terms of the coordinates of the vertices. However, this formula does not generalize to the 3D case. The general and simple formula (15) is thus adopted in this work, while clearly this part of the model can be replaced by another suitable formulation.

The unit normal vector $\boldsymbol{N}^e$ is calculated as the normalized gradient of the level-set function ϕ^h at the element centre $\boldsymbol{X}_0^e$,

$$\boldsymbol{N}^e = \frac{\nabla \phi^h(\boldsymbol{X}_0^e)}{\|\nabla \phi^h(\boldsymbol{X}_0^e)\|}. \tag{16}$$

Again, other options are here possible, including, for instance, determination of the normal individually at each Gauss integration point. According to our preliminary studies, such modifications have a minor effect on the results, and in this work we adopt the simple approach described above.

Knowing the volume fraction and the interface normal, the overall constitutive response of the laminate can be readily obtained by applying the micro-to-macro transition, as described in Section 2.2.

The above construction, Eqs. (15) and (16), is applicable when the element is cut by one interface only. The approach can be generalized to the case of more interfaces (and more phases) by introducing additional level-set functions, each corresponding to one interface. A higher-rank laminate can then be considered with the micro-macro transition applied in a hierarchical manner or, if there are only two phases, a simple laminate can be considered with the volume fraction equal to the total volume fraction of the phases within the element and with the lamination orientation obtained by averaging those corresponding to each interface. The latter approach is employed in the example considered in Section 4.4.

4. Illustrative examples

Performance of LET is examined in this section through several numerical examples. In all examples, we use a regular quadrilateral (2D) or hexahedral (3D) mesh. In all cases, the results are compared to those obtained using two simple non-conforming mesh approaches that will be referred to as ELA (element-level assignment) and GPLA (Gauss-point-level assignment), see Fig. 2. Whenever applicable a conforming mesh is also used.

As illustrated in Fig. 2(b), in ELA, the whole element is assigned to one of the phases, and this approach, sometimes called digital-image-based FEM or voxel-based FEM, is commonly used for segmented 2D and 3D images of the microstructure or for rasterized representation of the microstructure, e.g. [32–34]. In GPLA, Fig. 2(c), individual integration (Gauss) points are assigned to one of the phases according to the position of the integration point, possibly combined with an increased number of integration points, e.g. [7,17]. In the context of voids and free boundaries, this latter approach is closely related to the finite cell method [35].

Finite-element implementation and computations have been performed using the *AceGen/AceFEM* system [36,37], see also Appendix A.

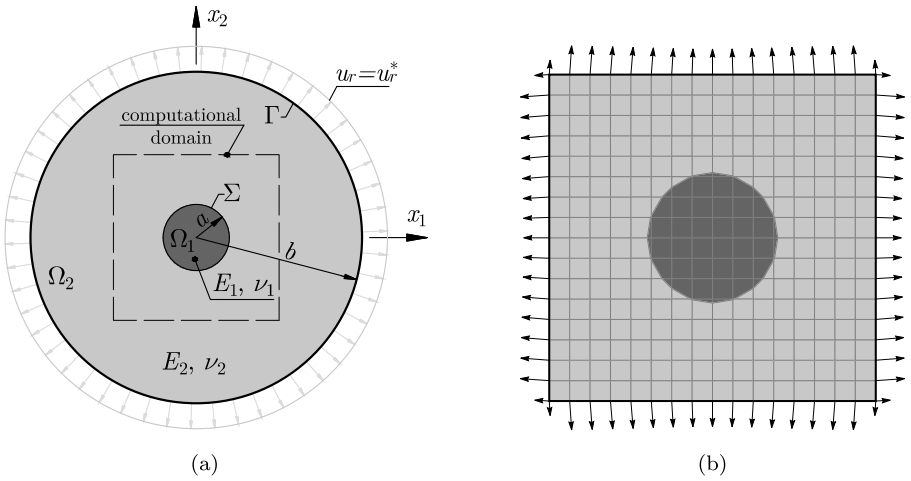

Fig. 3. Elastic inclusion problem: (a) scheme of the problem; (b) computational domain with a regular (non-conforming) mesh of quadrilateral elements (16×16 elements, $h = 0.125$). The interface Σ is approximated by the zero level set, $\phi^h = 0$. The arrows in panel (b) represent the nodal forces applied to the boundary nodes, which are calculated from the traction resulting from the analytical solution.

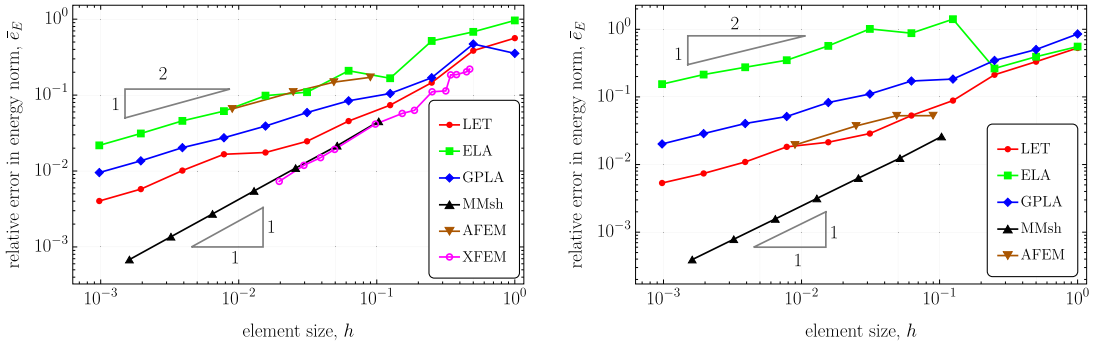

Fig. 4. Elastic inclusion problem: rate of convergence in energy norm for (a) soft inclusion ($E_2/E_1 = 10$) and (b) hard inclusion ($E_2/E_1 = 0.005$). The results obtained for a matching mesh of four-node quadrilateral elements are labelled 'MMsh'. The results for X-FEM are taken from [7], and those for A-FEM from [17].

4.1. Elastic inclusion

In this section, a 2D elastic inclusion problem in the small-strain framework is considered. The problem is adopted from [5,7]. Fig. 3(a) shows a body that consists of two domains, Ω_1 (inclusion) and Ω_2, with the elastic constants (E_1, ν_1) and (E_2, ν_2) that are constant within each domain and suffer discontinuity at the (bonded) interface Σ. The radius of the inclusion and the outer radius are denoted by a and b, respectively. The loading is applied by prescribing the radial displacement $u_r = u_r^*$ and zero circumferential displacement $u_\theta = 0$ at the outer boundary Γ. This problem admits an analytical solution that can be found in [5].

In the computational model, a square-shaped domain with the inclusion in the centre is considered, which is discretized into a regular mesh of isoparametric four-node elements. The dimensions of the computational domain are $L \times L$, where $L = 2$, while the parameters specifying the reference problem are adopted as $a = 0.4$ and $b = 2$. To ensure equivalence with the model described above, the traction resulting from the analytical solution is applied on the boundary of the computational domain. Additionally, appropriate displacement boundary conditions are imposed to prevent rigid-body motion.

To examine the performance of LET, the problem is solved for several mesh densities with the element size h varying between $h = 1$ (very coarse mesh with 2×2 elements) and $h \approx 0.001$ (2048×2048 elements). The elastic constants are adopted as $E_1 = 1$, $\nu_1 = 0.25$, $E_2 = 10$, and $\nu_2 = 0.3$ ('soft inclusion' case) and as $E_1 = 200$, $\nu_1 = 0.25$, $E_2 = 1$, and $\nu_2 = 0.3$ ('hard inclusion' case). Convergence of the error is shown in Fig. 4. The error is here defined as the relative error in energy norm, as in [7,17],

$$\bar{e}_E = \frac{1}{\left(\int_\Omega 2W(\boldsymbol{\varepsilon}^{\text{exact}})\,\mathrm{d}\Omega\right)^{1/2}} \left\| \boldsymbol{u}^h - \boldsymbol{u}^{\text{exact}} \right\|_{E(\Omega)} = \left(\frac{\int_\Omega W(\boldsymbol{\varepsilon}^h - \boldsymbol{\varepsilon}^{\text{exact}})\,\mathrm{d}\Omega}{\int_\Omega W(\boldsymbol{\varepsilon}^{\text{exact}})\,\mathrm{d}\Omega} \right)^{1/2}, \tag{17}$$

where W is the elastic strain energy density function, $\boldsymbol{u}^{\text{exact}}$ and $\boldsymbol{\varepsilon}^{\text{exact}}$ are the exact displacement and strain obtained from the analytical solution, and $\boldsymbol{u}^h$ and $\boldsymbol{\varepsilon}^h$ are the displacement and strain resulting from the computational model. The integrals are evaluated by applying the 2×2 Gauss quadrature. Note that, in the case of LET, the local strains in each phase are known at the Gauss points of the laminated elements, and the respective local strains are used to evaluate the error.

Fig. 4 shows the results obtained for LET, and for comparison, for ELA and GPLA, the two simple non-conforming mesh approaches that will be used as a reference in all subsequent examples. Fig. 4 includes also the results obtained for a matching mesh as well as the results taken from the literature for exactly the same problem, specifically, for X-FEM [7] (available only for the soft inclusion case) and for A-FEM [17]. It follows from Fig. 4 that the convergence rate of LET, ELA, GPLA, and A-FEM is similar, approximately equal to 0.5, but the error is the lowest for LET (in the hard inclusion case, the error of LET and A-FEM is similar). Since these methods employ a non-conforming approximation of the displacement field, the optimal convergence rate of 1, characteristic for

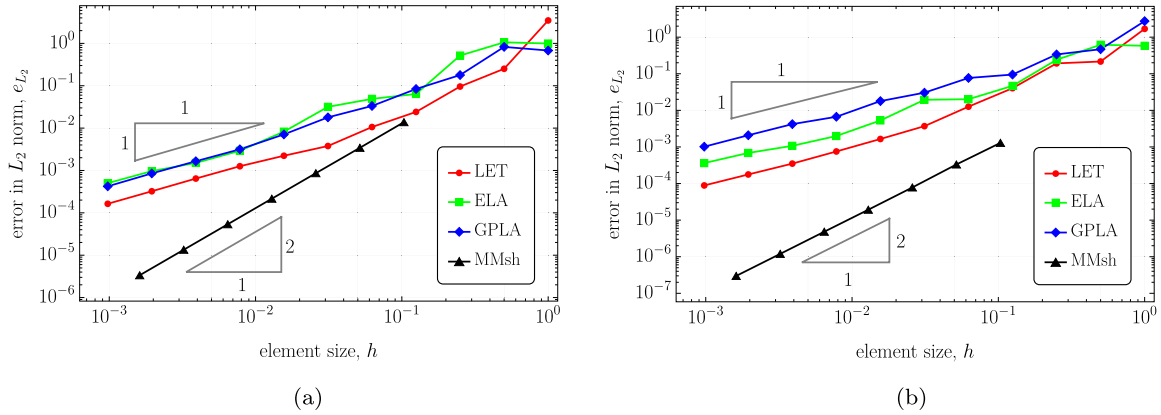

Fig. 5. Elastic inclusion problem: rate of convergence in L_2 norm for (a) soft inclusion ($E_2/E_1 = 10$) and (b) hard inclusion ($E_2/E_1 = 0.005$).

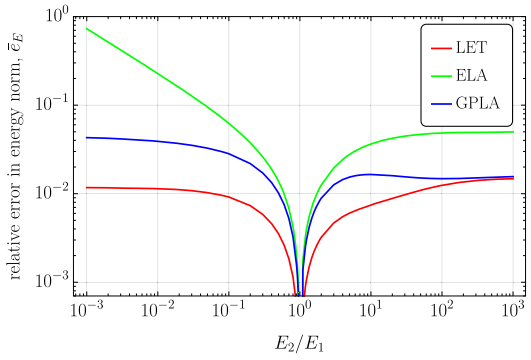

Fig. 6. Elastic inclusion problem: relative error in energy norm as a function of the Young's moduli contrast E_2/E_1.

a matching mesh and also for X-FEM, cannot be achieved. This is also illustrated in Fig. 5 where the error in L_2 norm ($e_{L_2} = \|\boldsymbol{u}^h - \boldsymbol{u}^{\text{exact}}\|_{L_2(\Omega)}$) is shown. In this norm, the convergence rate is approximately equal to 1 for LET, ELA and GPLA, while it is equal to 2 for a matching mesh, as expected. It is stressed here that LET is not aimed to compete with more sophisticated methods, like X-FEM, in terms of accuracy. The advantage of LET is its simplicity and ease of implementation, and, at the same time, improved accuracy, as compared to ELA and GPLA.

Fig. 6 shows the relative error in energy norm as a function of the Young's moduli contrast E_2/E_1 evaluated for $E_1 = 1$ and $\nu_1 = \nu_2 = 0.25$, and for the element size $h = 0.004$ (500×500 elements). Again, the error is the lowest for LET, and the difference with respect to ELA and GPLA increases with increasing contrast, particularly in the case of hard inclusion ($E_2/E_1 < 1$).

The results reported so far concern the overall error. However, in some situations, the local error can also be important, for instance, the artificial stress concentrations resulting from the non-conforming representation of interfaces. To illustrate the respective performance of LET, ELA and GPLA, Fig. 7 presents the difference between the exact local stresses and those predicted by the three methods for the soft-inclusion problem and for a representative mesh density (128×128 elements). Specifically, the equivalent (von Mises) stress σ_{eq} is considered and the difference is normalized by the maximum stress in the analytical solution, $\sigma^{\text{exact}}_{\text{eq,max}}$. Note that the colour scale in Fig. 7 corresponds to the range of values between 0 and 0.01, while the respective maximum values are significantly higher and are provided below each figure. In LET, in the laminated elements, the local stresses in each phase are considered (marked as 'micro') as well as the overall stress of the laminate (marked as 'macro'). It follows that LET performs much better than ELA and GPLA in representing the local stresses in each phase (the maximum difference is 0.131 in the case of LET-micro as compared to 0.898 for ELA and 1.395 for GPLA). In the case of the overall stress in LET, the maximum difference (0.754 for LET-macro) is only slightly smaller than in the case of ELA and GPLA.

4.2. Compatible eigenstrain at a planar interface

In this section we investigate the behaviour of LET for a 2D problem of elasticity with eigenstrain in the small-strain framework. Two elastic domains are separated by a planar interface inclined at an angle α to the horizontal axis, see Fig. 8(a). Each domain is homogeneous and is characterized by elastic constants E_i and ν_i and by a homogeneous eigenstrain $\boldsymbol{\varepsilon}^0_i$ so that the elastic strain energy is a function of the elastic strain, $W_i = W_i(\boldsymbol{\varepsilon}^{\text{e}})$, $\boldsymbol{\varepsilon}^{\text{e}} = \boldsymbol{\varepsilon} - \boldsymbol{\varepsilon}^0_i$.

The eigenstrains in both phases are assumed compatible so that

$$\Delta\boldsymbol{\varepsilon} = \boldsymbol{\varepsilon}^0_2 - \boldsymbol{\varepsilon}^0_1 = \frac{1}{2}\left(\boldsymbol{a} \otimes \boldsymbol{n} + \boldsymbol{n} \otimes \boldsymbol{a}\right), \tag{18}$$

where $\boldsymbol{n}$ is a unit normal to the interface, $\boldsymbol{a}$ is a prescribed vector, and to fix attention we assume that $\boldsymbol{\varepsilon}^0_1 = \boldsymbol{0}$. Accordingly, in the continuum setting, the total elastic strain energy vanishes,

$$\int_\Omega W(\boldsymbol{\varepsilon} - \boldsymbol{\varepsilon}^0)\,\mathrm{d}\Omega = 0. \tag{19}$$

For a non-conforming finite-element mesh, the local incompatibilities introduced by the discretization are accommodated by elastic strains which are localized along the interface and vanish far from the interface in view of the overall compatibility of the eigenstrains, cf. Eq. (18). This is illustrated in Fig. 8(c) which shows the normalized elastic strain energy density, $W/(a^2E^*)$, for a representative case of $\alpha = \pi/9$ and $\beta = \pi/2$ (a coarse mesh is used for illustration purposes). It can be seen that the elastic strain energy is visibly lower in case of LET than in case of ELA and GPLA.

The corresponding total strain energy can be used as a measure of the error. The normalized error in energy norm is thus defined as

$$\tilde{e}_E = \frac{1}{\left(a^2E^*L\right)^{1/2}}\left\|\boldsymbol{u}^h - \boldsymbol{u}^{\text{exact}}\right\|_{E(\Omega)} = \left(\frac{1}{a^2E^*L}\int_\Omega W(\boldsymbol{\varepsilon}^h - \boldsymbol{\varepsilon}^0)\,\mathrm{d}\Omega\right)^{1/2}, \tag{20}$$

where the error is normalized by the interface length L and also by $a = \|\boldsymbol{a}\|$ and $E^* = \sqrt{E_1E_2}$ so that the error does not depend on a and depends on E_1 and E_2 only through their ratio, the contrast E_2/E_1.

The analysis is performed for a wide range of Young's moduli contrasts $E_2/E_1 \in (0.001, 1000)$ with $\nu_1 = \nu_2 = 0.25$ and for two values of the angle β between vectors $\boldsymbol{a}$ and $\boldsymbol{n}$, namely $\beta = 0$ and $\beta = \pi/2$. The actual computations are carried out for $E_1E_2 = 1$ and $a = 1$. Dimensions of the rectangular domain are $w = 10$ and $h = 15$, and the domain is discretized into a regular mesh of 101×151 elements (element size $h \approx 0.1$). An odd number of elements is adopted in each direction and the interface passes

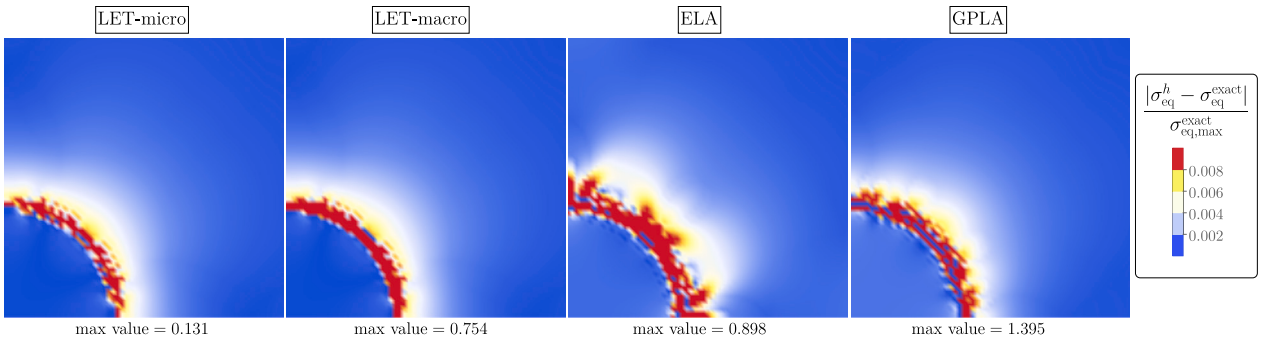

Fig. 7. Elastic inclusion problem: the difference between the exact local equivalent stress and that predicted by LET, ELA and GPLA normalized by the maximum stress $\sigma^{\rm exact}_{\rm eq,max}$ (soft inclusion, 128×128 elements, one quarter of the domain is shown).

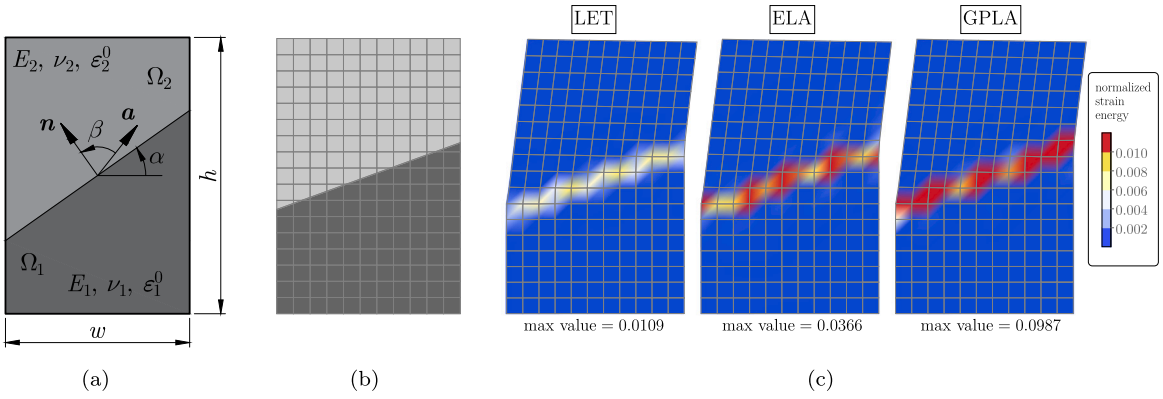

Fig. 8. Eigenstrain problem: (a) scheme of the problem; (b) computational domain with a coarse (non-conforming) mesh of 11×17 quadrilateral elements for a sample interface orientation $\alpha = \pi/9$ (the actual computations are carried out for a fine mesh of 101×151 elements); (c) deformed coarse mesh with a colour map of the normalized elastic strain energy density, $W/(a^2 E^*)$, for $\beta = \pi/2$ (displacements are scaled for better visibility).

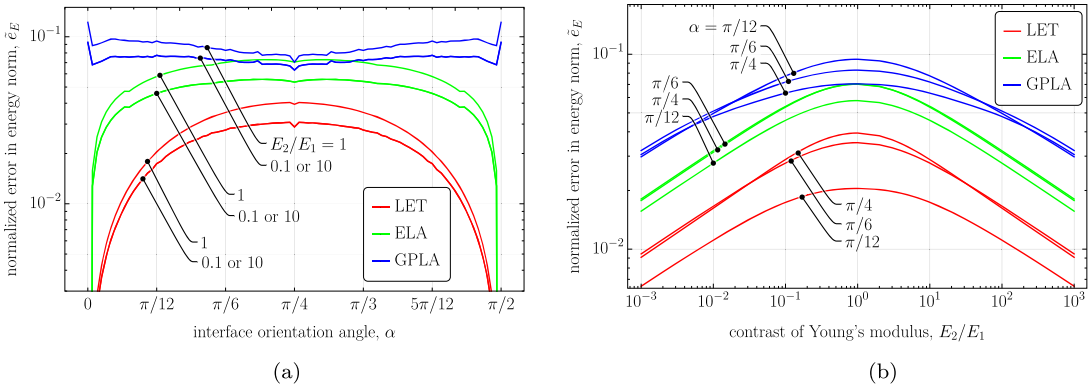

Fig. 9. Normalized error in energy norm for $\beta = 0$ as a function of: (a) the interface orientation angle α and (b) the Young's moduli contrast E_2/E_1.

through the centre of the domain so that, for all orientation angles, the mesh is non-conforming (also for $\alpha = 0$ and $\pi/2$). The boundaries are free, only the rigid body motion is prevented by enforcing adequate boundary conditions.

Representative results are shown in Fig. 9 for $\beta = 0$ and in Fig. 10 for $\beta = \pi/2$. Intermediate values of β are not considered since the corresponding solutions can be obtained by the superposition of those for $\beta = 0$ and $\beta = \pi/2$ (even if the error, as a nonlinear function of the solution, cannot be obtained by superposition).

Figs. 9(a) and 10(a) show the dependence of the error on the interface orientation angle α. As expected, the individual diagrams exhibit symmetry with respect to $\alpha = \pi/4$. Likewise, the diagrams in Figs. 9(b) and 10(b), which depict the dependence on the contrast E_2/E_1 exhibit symmetry with respect to $E_2/E_1 = 1$ (recall that $\nu_1 = \nu_2$ and $E_1 E_2 = 1$). It is also seen that, for LET and ELA, the error vanishes for $\alpha = 0$ and $\pi/2$, i.e., when the interface is parallel to element edges.

Figs. 9 and 10 show that in most cases the error is the lowest for LET. However, for $\beta = \pi/2$, when the eigenstrain jump is a shear strain, LET performs better than ELA and GPLA only for moderate contrasts, see Fig. 10(b).

4.3. Elastic inclusion with varying radius

One of the advantages of LET over ELA and GPLA is its ability to adapt to continuous changes in the position of the interface within a single finite element. In LET, if the position of the interface is varied in a continuous manner, the volume fractions of the phases and the orientation of the interface also change in a continuous manner, whereas in ELA and GPLA these changes are taken into account in a step-wise

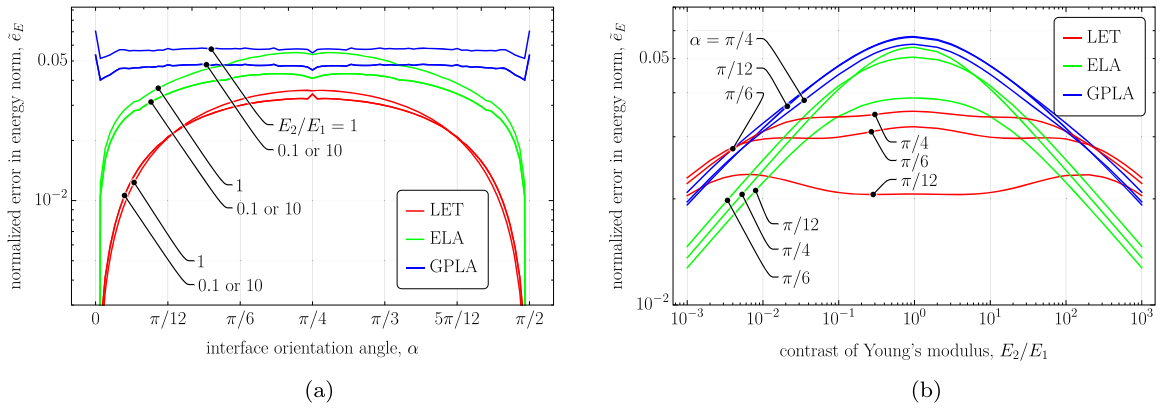

Fig. 10. Normalized error in energy norm for $\beta = \pi/2$ as a function of: (a) the interface orientation angle α and (b) the Young's moduli contrast E_2/E_1.

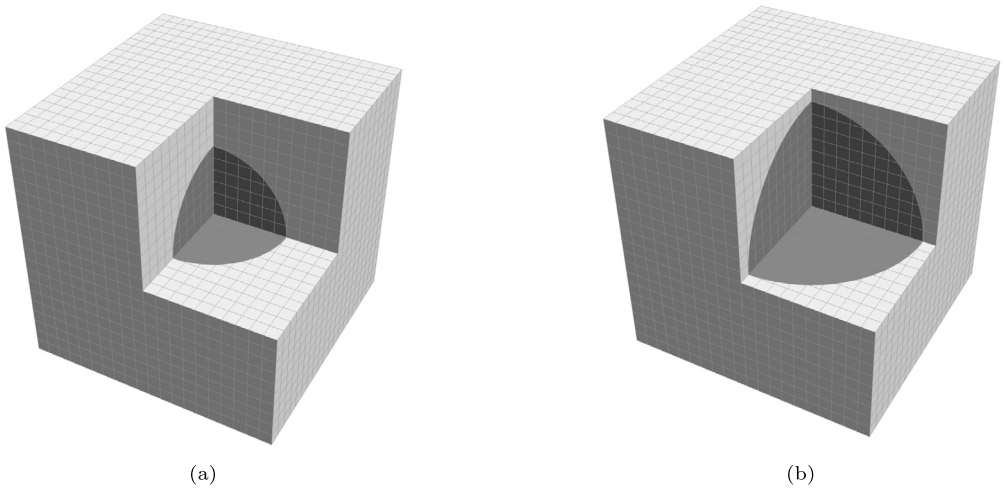

Fig. 11. Periodic unit cell with a spherical elastic inclusion of the diameter that varies between $D/L = 0.6$ (a) and $D/L = 0.9$ (b). A fixed regular finite-element mesh ($20 \times 20 \times 20$ elements) is used.

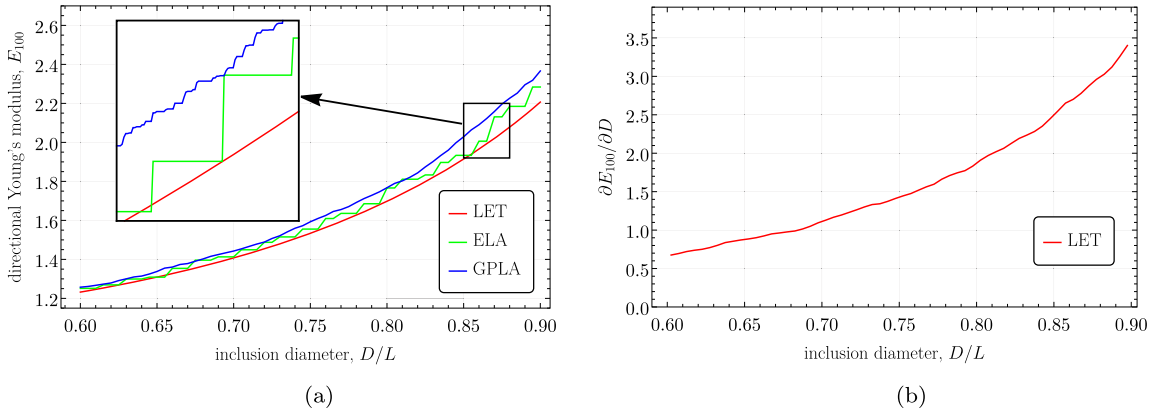

Fig. 12. (a) Dependence of the directional Young's modulus, E_{100}, on the inclusion diameter D. The inset shows the results computed with a finer step so that the jumps are clearly visible for both ELA and GPLA. (b) Dependence of the derivative of the directional Young's modulus, $\partial E_{100}/\partial D$, on the inclusion diameter D.

manner (volume fraction) or not at all (orientation of the interface). This effect is illustrated here by considering a 3D cubic cell of dimension L with a central inclusion of varying diameter D.

Both phases are linear elastic with the properties specified as $E_1 = 10$, $\nu_1 = 0.3$ (inclusion) and $E_2 = 1$, $\nu_2 = 0.2$ (matrix). The inclusion diameter is varied between $D/L = 0.6$ and $D/L = 0.9$, and a regular mesh of $20 \times 20 \times 20$ elements is used, see Fig. 11. Periodic boundary conditions are enforced and the overall elastic moduli tensor is determined in a standard manner by subjecting the unit cell to 6 linearly independent macroscopic strains (actually 3 are sufficient due to symmetry). The overall elastic moduli tensor is then determined in terms of the resulting overall stress tensors. Below, the results are reported in terms of the directional Young's modulus $E_{100} = (S_{1111})^{-1}$, where S_{ijkl} denotes the components of the elastic compliance tensor.

Fig. 12(a) shows the dependence of E_{100} on the inclusion diameter. The mesh is here rather coarse, hence the predictions of the three methods (LET, ELA, GPLA) differ visibly. However, the important difference is that the dependence is smooth in the case of LET, while in the case

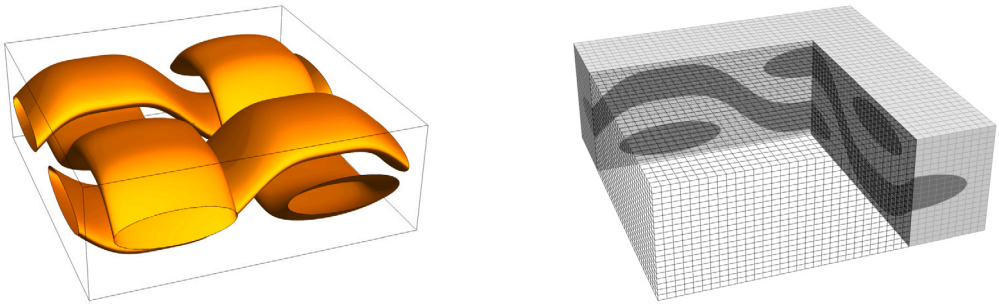

(a) (b)

Fig. 13. Periodic woven-cell problem: (a) geometry, (b) finite-element mesh ($40\times40\times20$ elements).

of ELA and GPLA the overall properties change in a step-wise manner, see the inset in Fig. 12(a). Here, the overall moduli (e.g., E_{100}) exhibit a jump whenever the element (for ELA) or Gauss point (for GPLA) is assigned to a different phase when the interface position is changed. Clearly, LET is free of such artifacts, and the overall moduli depend on the inclusion diameter in a continuous fashion.

For completeness, the derivative of the dependence of E_{100} on D, as predicted by LET, is shown Fig. 12(b). The derivative is here computed using the finite difference scheme in terms of two subsequent data points. The small irregularities that can be seen in Fig. 12(b) result from the error introduced by LET. It follows that the response is continuous and its derivative is meaningful, which suggests that LET can be considered as a candidate for treating moving interface problems, such as microstructure evolution or shape optimization.

4.4. Hyperelastic woven microstructure

In this example, unlike the previous ones, the internal geometry is more complex, and for this reason the real advantage of LET over conforming-mesh discretization can be appreciated. The model consists of a 3D periodic cell of the dimensions $L\times L\times H=2\times2\times0.7$, in which four interlaced fibres are immersed in the matrix, Fig. 13.

For a coarse mesh, it may happen that one element is cut by two interfaces. Accordingly, as commented in Section 3, a separate level-set function is introduced for each fibre. If an element is cut by two interfaces, so that it contains portions of the matrix and two fibres, the total volume fraction of the fibres is simply taken as the sum of the volume fractions of the individual fibres and the lamination orientation is determined by averaging those determined individually for each interface.

The geometry of the fibres aligned with the x_2-axis is defined by the centreline $(\pm x_1^0, x_2, \mp x_3^0(x_2))$ parameterized by x_2 and by the elliptical cross-section (in the (x_1,x_3)-plane) specified by the following inequality

$$\sqrt{\left(\frac{x_1\pm x_1^0}{a}\right)^2+\left(\frac{x_3\pm x_3^0(x_2)}{b}\right)^2}-1\leqslant0, \tag{21}$$

where $a=0.35$ and $b=0.11$ are the semi-major and semi-minor axes of the ellipse, $x_1^0=L/4$ defines the offset between the fibres in the x_1-direction, function $x_3^0(y)$ is specified as

$$x_3^0(x_2)=A\left(\frac{9}{8}\sin\left(\frac{2\pi x_2}{L}\right)+\frac{1}{8}\sin\left(\frac{6\pi x_2}{L}\right)\right), \tag{22}$$

and $A=0.2$ is the amplitude of the function $x_3^0(x_2)$. The origin of the coordinate system is located at the centre of the unit cell. The geometry of the fibres aligned with the x_1-axis is defined analogously.

The finite-deformation framework is employed, and both the matrix and the fibres are assumed to be hyperelastic, characterized by a compressible neo-Hookean strain energy function. The elastic properties are specified as $E_1=100$ (fibres), $E_2=1$ (matrix), and $\nu_1=\nu_2=0.45$.

Periodic boundary conditions are imposed and loading is applied by prescribing the overall deformation gradient $\bar{\boldsymbol{F}}$. Three deformation modes are considered, namely isochoric tension and two cases of simple shear. The isochoric tension along the x_1-axis is specified by

$$\bar{\boldsymbol{F}}=(1+\epsilon)\boldsymbol{e}_1\otimes\boldsymbol{e}_1+\frac{1}{\sqrt{1+\epsilon}}\left(\boldsymbol{e}_2\otimes\boldsymbol{e}_2+\boldsymbol{e}_3\otimes\boldsymbol{e}_3\right), \tag{23}$$

where ϵ denotes the elongation, and $\boldsymbol{e}_i$ are the orthonormal basis vectors. The simple shear is specified by

$$\bar{\boldsymbol{F}}=\boldsymbol{I}+\gamma\,\boldsymbol{s}\otimes\boldsymbol{n}, \tag{24}$$

with $\boldsymbol{s}=\boldsymbol{e}_1$ and $\boldsymbol{n}=\boldsymbol{e}_2$ (case #1) and $\boldsymbol{s}=\frac{1}{\sqrt{2}}(\boldsymbol{e}_1+\boldsymbol{e}_2)$ and $\boldsymbol{n}=\frac{1}{\sqrt{2}}(\boldsymbol{e}_2-\boldsymbol{e}_1)$ (case #2).

In the convergence studies reported below, a family of regular meshes of hexahedral elements is used with 10 to 40 elements along the x_1- and x_2-directions (element size h varies between 0.2 and 0.05) and with 5 to 20 elements in the x_3-direction, respectively. As a reference, the results obtained for a fine mesh of $80\times80\times40$ elements ($h=0.025$) are used, and both LET and ELA are employed for this purpose (the two methods give very similar results; for ELA, in the simple shear case #2, the solution could not be achieved at the maximum load due to convergence problems). The F-bar formulation is employed to avoid volumetric locking effects [38]. Fig. 14 illustrates the three deformation modes for the mesh of $40\times40\times20$ elements.

The overall stress–strain response predicted using the $20\times20\times10$ mesh is shown in Fig. 15. In the case of isochoric tension, the $\bar{\sigma}_{11}$ component of the overall Cauchy stress $\bar{\boldsymbol{\sigma}}$ is shown as a function of the overall elongation ϵ, Fig. 15(a). In the case of simple shear, the shear stress $\bar{\tau}=\boldsymbol{s}\cdot\bar{\boldsymbol{\sigma}}\cdot\boldsymbol{n}$ is shown as a function of the overall shear γ, Fig. 15(b,c). Results obtained for a four times finer mesh are included in Fig. 15 as a reference.

In Fig. 15, the mesh is relatively coarse, hence the visible differences between the three methods (LET, ELA, GPLA). In all cases, GPLA delivers the stiffest response, with the largest error with respect to the reference results. The remaining two methods (LET and ELA) deliver similar results that agree well with the reference ones, except for simple-shear case #1, where the LET results are visibly stiffer. Accordingly, for this specific mesh density ($h=0.1$), ELA seems to perform the best. However, this conclusion does not apply to other mesh densities, as illustrated below.

Fig. 16 shows the overall stress at the maximum strain as a function of the mesh size h. It follows that predictions of LET are stable (i.e., reasonably close to the reference solution) over the entire range of mesh densities studied. Likewise, GPLA delivers stable results, although with a significantly higher error. On the other hand, ELA performs badly for coarser meshes, which is associated with a poor representation of the internal geometry by ELA.

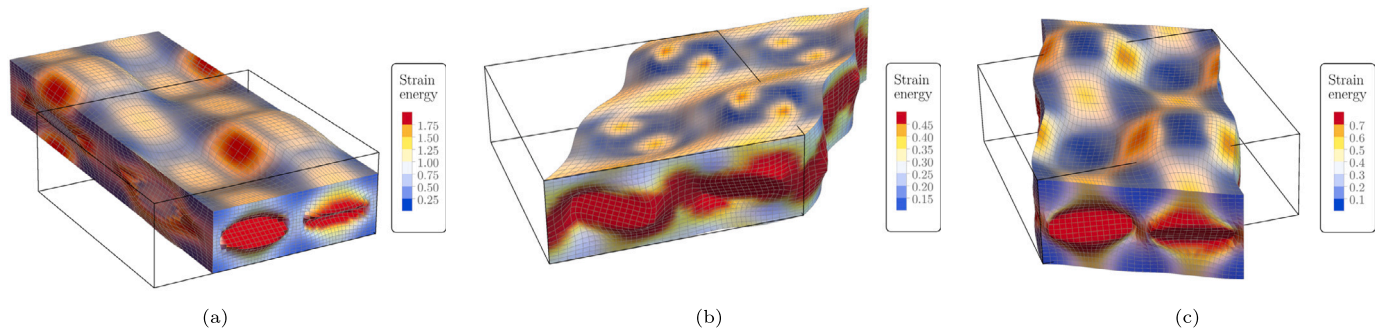

Fig. 14. Woven cell: deformed configuration for (a) isochoric tension ($\epsilon = 0.8$), (b) simple shear (case #1, $\gamma = 0.7$), and (c) simple shear (case #2, $\gamma = 0.7$). Colour maps show the elastic strain energy density W.

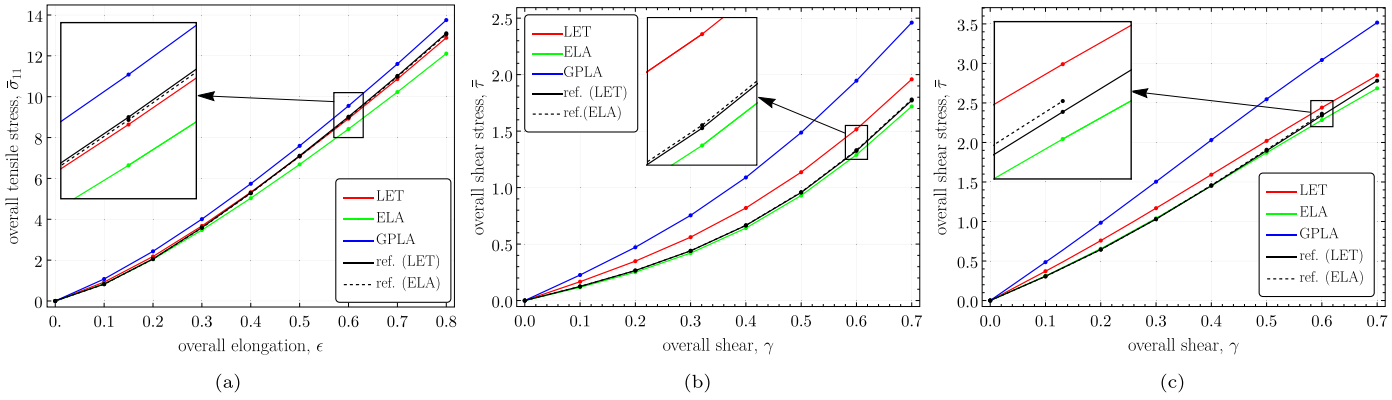

Fig. 15. Woven cell: overall stress–strain response for (a) isochoric tension, (b) simple shear (case #1), and (c) simple shear (case #2). The results correspond to the mesh of $20 \times 20 \times 10$ elements (element size $h = 0.1$). As a reference, the LET and ELA results obtained for a fine mesh ($80 \times 80 \times 40$ elements, $h = 0.025$) are used.

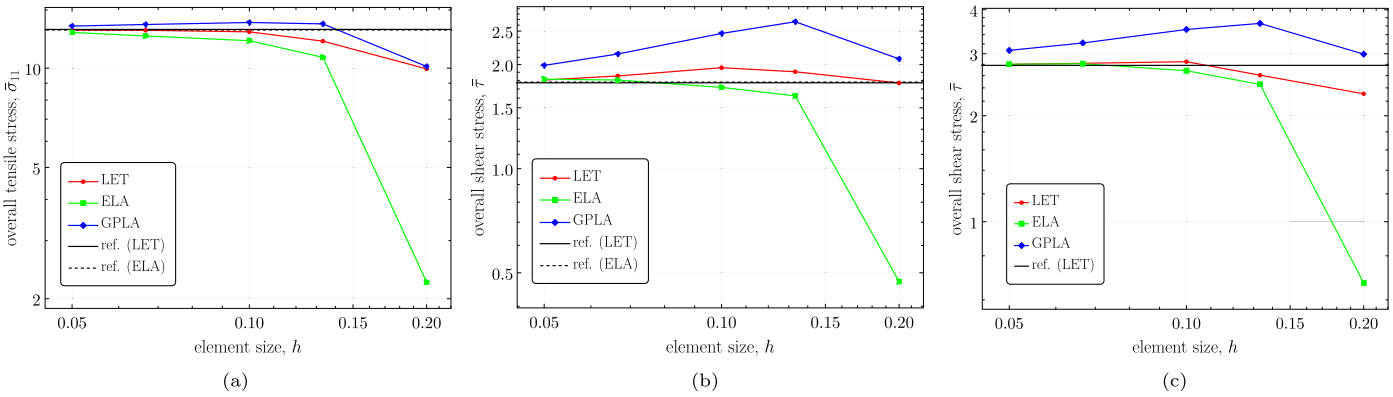

Fig. 16. Woven cell: convergence of the overall stress (at the maximum strain, see Fig. 15) with element size h for (a) isochoric tension, (b) simple shear (case #1), and (c) simple shear (case #2). As a reference, the LET and ELA results obtained for a fine mesh ($80 \times 80 \times 40$ elements, $h = 0.025$) are used.

4.5. Elasto-plastic composite

In this example, we consider a 2D periodic unit cell with a circular inclusion. Both phases are elastic-plastic and plane-strain conditions are assumed. In the continuum setting, the position of the inclusion within the unit cell is arbitrary in view of periodicity, and it does not affect the overall response. This is not the case in the discrete setting when the position of the inclusion with respect to the finite-element mesh is an additional geometric feature that may affect the response, as revealed by our preliminary studies. Accordingly, in this section we examine this effect in detail. Specifically, the overall response under simple shear is studied for 100 randomly selected positions of the inclusion and for a family of regular meshes of $N \times N$ elements with $N = 2, 4, 8, \ldots, 256$. Below, for each method considered (LET, ELA, GPLA), the responses obtained for a given mesh density are averaged and compared to the reference ("exact") solution obtained using a high-resolution conforming mesh involving over 3 million elements. The standard deviation is also examined as an indicator of the sensitivity of the response to the position of the inclusion.

The geometric and material parameters adopted in this example are the following. The dimensions of the unit cell are $L \times L$ with $L = 2$, and the inclusion radius is $R = 0.6$. The finite-deformation framework is adopted and both phases are governed by the finite-strain J_2 plasticity model with linear isotropic hardening, see Appendix A for more details. The yield stress σ_y is thus specified by $\sigma_y(\alpha) = \sigma_y^0 + K\alpha$, where α denotes the accumulated plastic strain. The elastic properties of the matrix and inclusion are the same, $E = 70000$, $\nu = 0.25$, and so is the hardening modulus $K = 2000$. The initial yield stress of the inclusion, $\sigma_{y,1}^0 = 70$, is lower than that of the matrix, $\sigma_{y,2}^0 = 120$, which induces an inhomogeneous deformation within the unit cell once plastic deforma-

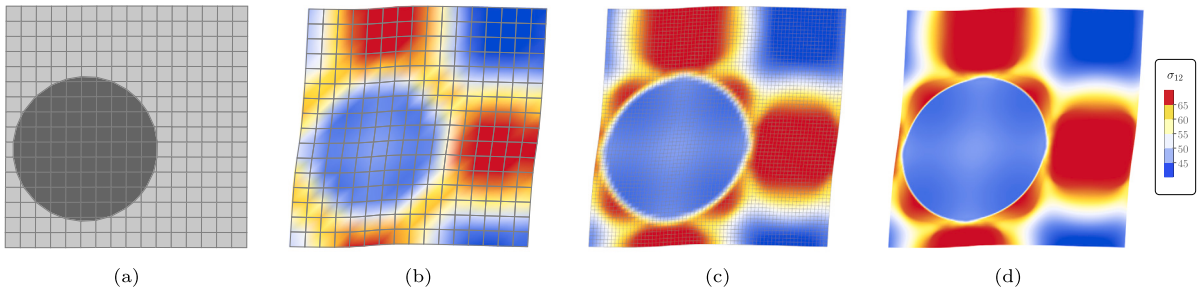

Fig. 17. Elasto-plastic composite: (a) 16×16 mesh with a randomly positioned circular inclusion; (b,c,d) deformed mesh (displacements scaled 20 times) with the distribution of the shear component σ_{12} of the Cauchy stress tensor for 16×16 (b), 64×64 (c) and 256×256 (d) mesh.

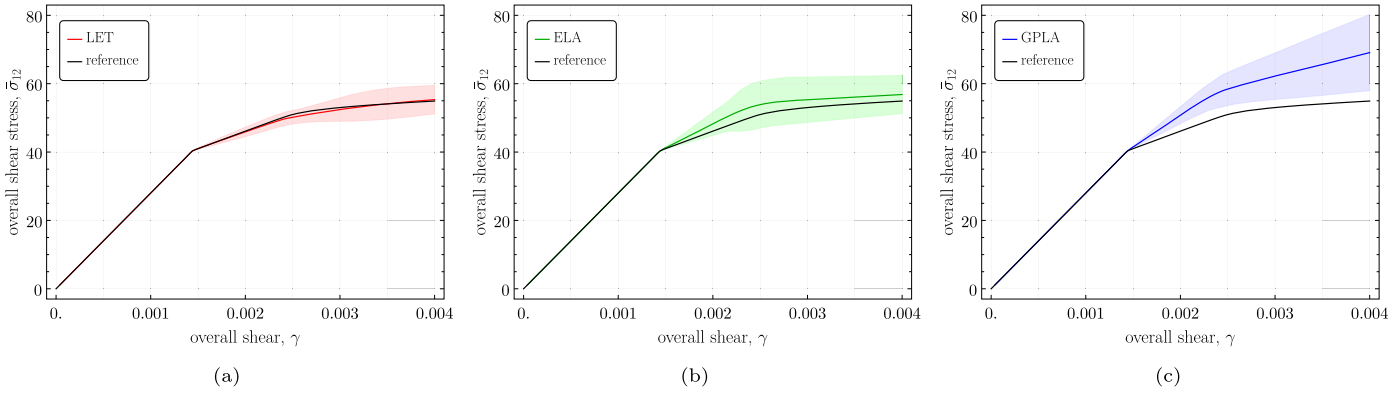

Fig. 18. Elasto-plastic composite: overall stress–strain ($\bar{\sigma}_{12}$–γ) response obtained for the 4×4 mesh (element size $h = 0.5$) and for LET (a), ELA (b) and GPLA (c). In each case, the average over 100 random inclusion positions is indicated by a solid line and the corresponding shaded area indicates the spread (±3 standard deviations).

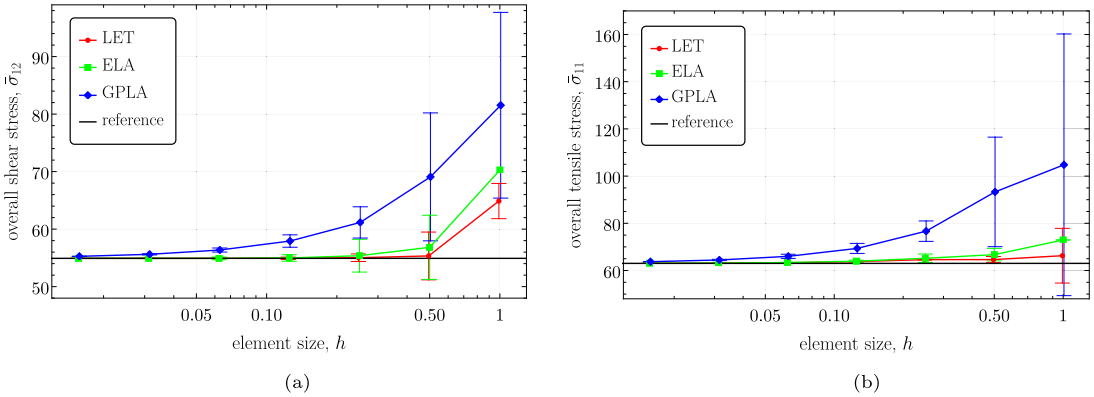

Fig. 19. Elasto-plastic composite: dependence of the average overall stress on the element size h for (a) simple shear (shown is the shear stress at $\gamma = 0.004$) and (b) isochoric tension (shown is the tensile stress at the elongation of 0.004). The error bars indicate the spread (±3 standard deviations).

tion occurs. The computations have been carried out using a sufficiently small time step in order to accurately represent the overall response. Additional computations (not reported here) have been carried out using a large time step to examine the robustness and convergence properties of the computational scheme for elasto-plastic laminates described in Appendix A. The results show that the robustness and convergence of LET are essentially the same as those of ELA and GPLA.

The unit cell is loaded in simple shear by prescribing the overall deformation gradient $\bar{\boldsymbol{F}}$ according to Eq. (24) with $\boldsymbol{s} = \boldsymbol{e}_1$ and $\boldsymbol{n} = \boldsymbol{e}_2$. The initial stage of deformation is considered with the overall shear γ increasing from 0 to 0.004 so that the details of the elastic-to-plastic transition are revealed. A sample finite-element mesh with the inclusion at a sample position within the unit cell is shown in Fig. 17(a), and the deformation mode along with the shear component σ_{12} of the Cauchy stress tensor is shown in Fig. 17(b-d) for three selected mesh densities.

Fig. 18 shows the overall stress–strain response ($\bar{\sigma}_{12}$ component of the overall Cauchy stress as a function of the overall shear γ) for a coarse mesh of 4×4 elements. Here, the average response is compared to the reference solution and, moreover, the shaded area represents the spread of the individual responses corresponding to the randomly positioned inclusions (the width of the shaded area is set equal to ±3 standard deviations). Since the mesh is here coarse (4×4 elements), visible differences with respect to the reference solution are apparent. It can be seen that LET delivers the most accurate results in terms of both the average and the spread. The accuracy is visibly worse in the case of ELA and significantly worse in the case of GPLA.

Convergence of the results with mesh refinement is illustrated in Fig. 19. This figure, in addition to simple shear, includes also the results corresponding to isochoric tension (i.e., pure shear). In the case of LET and ELA, the averaged stress converges quickly to the reference

value, LET converging somewhat faster. However, in the case of LET, the spread vanishes significantly faster than in the case of ELA. Consistent with the other results, the accuracy of GPLA is the worse.

Note that in the case of ELA, the results obtained for the coarsest mesh considered (2×2 elements, $h = 1$) exhibit no spread, see Fig. 19. This is because in this case all elements are assigned to the matrix phase regardless of the position of the inclusion (and the unit cell is thus homogeneous).

5. Conclusion

A simple approach has been developed for an improved treatment of weak discontinuities for a non-conforming spatial discretization within the finite element method. The use of a non-conforming finite-element mesh has several advantages over the conforming one, in particular, in 3D and for complex geometries, but comes at the cost of loss of accuracy caused by an inexact representation of the geometry of the phases. The proposed approach is thus aimed at improving the accuracy while maintaining the simplicity such that implementation is carried out solely at the element level and no additional global degrees of freedom are introduced.

In the proposed laminated element technique (LET), each finite element that is cut by an interface is treated as a laminate of the two involved phases with the volume fractions of the phases equal to their volume fractions within the element and with the lamination orientation specified by the orientation of the interface. No treatment is applied to the remaining elements, i.e., those that are not cut by an interface. The approach is inspired by the composite voxel technique in FFT-based homogenization [24–29].

The approach is general in the sense that each phase may be governed by an arbitrary material model. The constitutive behaviour of each laminated element results from the closed-form, exact micro-to-macro transition relations for simple laminates. For nonlinear material behaviour (e.g., plasticity, finite deformations), a set of nonlinear equations must be solved at each Gauss point. This makes the effective constitutive model within the laminated elements somewhat more complex, but an efficient computational implementation is possible, including consistent linearization, as illustrated in the case of finite-strain plasticity.

Several numerical examples have been studied and the proposed approach has been shown to be, in most cases, superior in terms of accuracy to two alternative methods in which the whole element or individual Gauss points are assigned to a specific phase. However, the rate of convergence with mesh refinement is not improved, unlike in more sophisticated approaches, such as X-FEM. On the other hand, it is an important feature of the proposed approach that the response is a continuous function of the position of the interface, which opens a possibility of its application in various problems involving moving interfaces.

Declaration of competing interest

The authors declare that they have no known competing financial interests or personal relationships that could have appeared to influence the work reported in this paper.

Data availability

Data will be made available on request.

Acknowledgement

This work has been partially supported by the National Science Centre (NCN) in Poland through Grant No. 2018/29/B/ST8/00729.

Appendix A. Incremental computational scheme for an elastic-plastic simple laminate

In this appendix, we discuss the case of a simple laminate composed of two elastic-plastic materials. As discussed below, the corresponding computational model involves a nested iterative-subiterative Newton scheme. In the inner iterative loops, nonlinear incremental equations of plasticity are solved, thus yielding the local incremental response (stress) of each phase as a function of the respective local strain (deformation gradient). In the outer iterative loop, the jump vector $\boldsymbol{c}$, see Eq. (6), is found by solving the traction continuity equation (2). In general terms, the algorithm is the same as that used in [27] in the context of the composite voxel technique in FFT-based homogenization. Apart from the finite-deformation setting used here, the main difference is that the procedure described below includes the consistent linearization of the overall incremental response of the elastic-plastic laminate, which is missing in [27] as it is not needed in the usual FFT-based schemes. Exact consistent linearization is crucial in implicit FEM so that the Newton method can be effectively used on the structural level. In this work, the exact linearization is achieved by using the automatic differentiation (AD) technique that is available in *AceGen* [36,37], and below we use the compact AD-based notation introduced in [36].

The incremental constitutive equations of finite-strain plasticity are rather standard [39], and the details are omitted here. The specific AD-based formulation of elastoplasticity which is adopted here follows that developed in [36], see also [37,40]. On the other hand, the treatment of the laminated microstructure is based on that developed in [41] for the incremental Mori–Tanaka scheme (with due differences). The corresponding AD-based formulation is provided below in the form of a pseudocode with only short comments, while for the details the reader is referred to [41].

The AD-based notation employed in the pseudocodes below uses a special notation to denote the computational derivative, i.e., the derivative evaluated by AD. The computational derivative is denoted by $\hat{\delta} f / \hat{\delta} \mathbf{a}$, where f is a function defined by an algorithm (or computer program) in terms of independent variables collected in vector $\mathbf{a}$. The actual dependencies present in the algorithm can be overridden or modified by introducing the so-called AD exceptions that are denoted by a vertical bar following the derivative with additional specifications in the subscript. The details can be found in [36,37].

Adopting the finite-strain framework, the elastic strain energy of phase i is expressed as a function of the deformation gradient $\boldsymbol{F}_i = \boldsymbol{F}_i^{n+1}$ and the vector $\mathbf{h}_i = \mathbf{h}_i^{n+1}$ of internal (history) variables at the current time step $t = t_{n+1}$,

$$W_i = W_i(\boldsymbol{F}_i, \mathbf{h}_i), \tag{A.1}$$

and the Piola stress $\boldsymbol{P}_i = \boldsymbol{P}_i^{n+1}$ is thus given by

$$\boldsymbol{P}_i = \frac{\partial W_i(\boldsymbol{F}_i, \mathbf{h}_i)}{\partial \boldsymbol{F}_i}. \tag{A.2}$$

Here and below, the superscript $n+1$ denoting the quantities at t_{n+1} is omitted to make the notation more compact. Time-discrete evolution of the internal variables $\mathbf{h}_i$ is governed by a set of nonlinear equations written symbolically in the residual form as

$$\mathbf{Q}_i(\boldsymbol{F}_i, \mathbf{h}_i, \mathbf{h}_i^n) = \mathbf{0}, \tag{A.3}$$

where $\mathbf{h}_i^n$ denotes the known internal variables at the previous time step $t = t_n$. In computational plasticity, the incremental equations of elastoplasticity are usually solved using the return-mapping algorithm, which leads to the *state update algorithm* that is outlined in Algorithm 1 using the AD-based notation. In this algorithm, the local problem (A.3) is solved iteratively using the Newton method, and the derivative of the implicit dependence of the solution $\mathbf{h}_i$ on $\boldsymbol{F}_i$ (denoted by $\mathbf{G}_i$ in Algorithm 1) is computed in the standard manner [36,42],

$$\frac{\partial \mathbf{h}_i}{\partial \boldsymbol{F}_i} = -\left(\frac{\partial \mathbf{Q}_i}{\partial \mathbf{h}_i} \right)^{-1} \frac{\partial \mathbf{Q}_i}{\partial \boldsymbol{F}_i}. \tag{A.4}$$

Algorithm 1 `StateUpdate[ ]`: state update algorithm for phase i.

input: $\boldsymbol{F}_i$, $\mathbf{h}_i^n$
$\phi_i^{\text{trial}} \leftarrow \phi_i(\boldsymbol{F}_i, \mathbf{h}_i^n)$
if $\phi_i^{\text{trial}} < 0$ **then**
  $\mathbf{h}_i \leftarrow \mathbf{h}_i^n$
  $\mathbf{G}_i \leftarrow \mathbf{0}$
else
  $\mathbf{h}_i \leftarrow \mathbf{h}_i^n$
  repeat
    $\mathbf{A}_i \leftarrow \dfrac{\hat{\delta}\mathbf{Q}_i\left(\boldsymbol{F}_i, \mathbf{h}_i, \mathbf{h}_i^n\right)}{\hat{\delta}\mathbf{h}_i}$ ▷ tangent matrix, $\mathbf{A}_i = \dfrac{\partial \mathbf{Q}_i}{\partial \mathbf{h}_i}$
    $\Delta\mathbf{h}_i \leftarrow -\mathbf{A}_i^{-1}\mathbf{Q}_i$
    $\mathbf{h}_i \leftarrow \mathbf{h}_i + \Delta\mathbf{h}_i$
  until $\|\Delta\mathbf{h}_i\| \le tol$
  $\mathbf{G}_i \leftarrow -\mathbf{A}_i^{-1}\left.\dfrac{\hat{\delta}\mathbf{Q}_i}{\hat{\delta}\boldsymbol{F}_i}\right|_{\mathbf{h}_i=\text{const}}$ ▷ $\mathbf{G}_i = \dfrac{\partial \mathbf{h}_i}{\partial \boldsymbol{F}_i}$
end if
$\mathbf{h}_i \leftarrow \mathbf{h}_i\Big|_{\frac{\mathrm{D}\mathbf{h}_i}{\mathrm{D}\boldsymbol{F}_i}=\mathbf{G}_i}$ ▷ introduce the implicit dependence of $\mathbf{h}_i$ on $\boldsymbol{F}_i$
$\boldsymbol{P}_i \leftarrow \left.\dfrac{\hat{\delta}W_i(\boldsymbol{F}_i, \mathbf{h}_i)}{\hat{\delta}\boldsymbol{F}_i}\right|_{\mathbf{h}_i=\text{const}}$ ▷ AD exception ensures that $\boldsymbol{P}_i$ is computed correctly
return: $\mathbf{h}_i$, $\boldsymbol{P}_i$, $\mathbf{G}_i$

The specific constitutive functions of the finite-strain J_2 plasticity model used in this work, see Section 4.5, are summarized in Box 1, see the formulation I-C-C-b in Box 1 in [40]. Box 1 provides also the corresponding definitions of the vector of internal variables $\mathbf{h}_i$ and of the local residual $\mathbf{Q}_i$. For brevity, the subscript i is omitted in Box 1.

Box 1: Constitutive equations of finite-strain J_2 plasticity with isotropic hardening. Phase index i is omitted for brevity.

Given: $\boldsymbol{F}, \boldsymbol{C}_{\mathrm{p},n}^{-1}, \gamma_n$ Find: $\boldsymbol{C}_{\mathrm{p}}^{-1}, \gamma$

$\boldsymbol{b}_{\mathrm{e}} = \boldsymbol{F}\boldsymbol{C}_{\mathrm{p}}^{-1}\boldsymbol{F}^{\mathrm{T}}$
$I_1 = \operatorname{tr}\boldsymbol{b}_{\mathrm{e}}, \quad I_3 = \det\boldsymbol{b}_{\mathrm{e}}$
$W = \frac{1}{2}\mu\left(I_1 - 3 - \log I_3\right) + \frac{1}{4}\lambda\left(I_3 - 1 - \log I_3\right)$
$\boldsymbol{\tau} = 2\boldsymbol{b}_{\mathrm{e}}\dfrac{\partial W}{\partial \boldsymbol{b}_{\mathrm{e}}}$ ▷ automation: $\boldsymbol{\tau} \leftarrow 2\boldsymbol{b}_{\mathrm{e}}\dfrac{\hat{\delta}W_{\mathrm{e}}}{\hat{\delta}\boldsymbol{b}_{\mathrm{e}}}$
$\boldsymbol{\tau}' = \boldsymbol{\tau} - \frac{1}{3}(\operatorname{tr}\boldsymbol{\tau})\boldsymbol{I}$
$\phi = \sqrt{\frac{3}{2}\boldsymbol{\tau}'\cdot\boldsymbol{\tau}'} - \sigma_{\mathrm{y}}(\gamma)$
$\boldsymbol{n} = \dfrac{\partial\phi}{\partial\boldsymbol{\tau}}$ ▷ automation: $\boldsymbol{n} \leftarrow \dfrac{\hat{\delta}\phi}{\hat{\delta}\boldsymbol{\tau}}$
$\mathcal{Z} = \boldsymbol{F}\boldsymbol{C}_{\mathrm{p}}^{-1} - \exp\left(-2\left(\gamma - \gamma_n\right)\boldsymbol{n}\right)\boldsymbol{F}\boldsymbol{C}_{\mathrm{p},n}^{-1}$

$\mathbf{h} = \left\{C_{\mathrm{p},11}^{-1} - 1, C_{\mathrm{p},22}^{-1} - 1, C_{\mathrm{p},33}^{-1} - 1, C_{\mathrm{p},23}^{-1}, C_{\mathrm{p},13}^{-1}, C_{\mathrm{p},12}^{-1}, \gamma\right\}$
$\mathbf{Q} = \left\{\mathcal{Z}_{11}, \mathcal{Z}_{22}, \mathcal{Z}_{33}, \mathcal{Z}_{23}, \mathcal{Z}_{13}, \mathcal{Z}_{12}, \phi\right\}$

Consider now a simple laminate in which both phases are governed by an elastic-plastic material model. Expressing the local deformation gradients in terms of $\bar{\boldsymbol{F}}$ and $\boldsymbol{c}$, as in Eq. (6), the macroscopic elastic strain energy $\bar{W} = \langle W \rangle$ reads

$$\bar{W}(\bar{\boldsymbol{F}}, \boldsymbol{c}, \mathbf{h}_1, \mathbf{h}_2) = (1-\eta)W_1(\boldsymbol{F}_1, \mathbf{h}_1) + \eta W_2(\boldsymbol{F}_2, \mathbf{h}_2), \tag{A.5}$$

and the macroscopic stress is obtained as

$$\bar{\boldsymbol{P}} = \frac{\partial\bar{W}(\bar{\boldsymbol{F}}, \boldsymbol{c}, \mathbf{h}_1, \mathbf{h}_2)}{\partial\bar{\boldsymbol{F}}} = (1-\eta)\frac{\partial W_1}{\partial\boldsymbol{F}_1}\frac{\partial\boldsymbol{F}_1}{\partial\bar{\boldsymbol{F}}} + \eta\frac{\partial W_2}{\partial\boldsymbol{F}_2}\frac{\partial\boldsymbol{F}_2}{\partial\bar{\boldsymbol{F}}} = (1-\eta)\boldsymbol{P}_1 + \eta\boldsymbol{P}_2. \tag{A.6}$$

The unknown vector $\boldsymbol{c}$ is obtained by solving, using the Newton method, the compatibility condition (2) written here in the residual form as

$$\mathbf{R}(\bar{\boldsymbol{F}}, \boldsymbol{c}, \mathbf{h}_1, \mathbf{h}_2) = (\boldsymbol{P}_2 - \boldsymbol{P}_1)\boldsymbol{N} = \mathbf{0}, \tag{A.7}$$

where the internal variables $\mathbf{h}_i$ depend on $\boldsymbol{c}$ through $\boldsymbol{F}_i$, thus $\mathbf{h}_i = \mathbf{h}_i(\boldsymbol{F}_i(\bar{\boldsymbol{F}}, \boldsymbol{c}))$, and this dependence must be taken into account when the residual $\mathbf{R}$ is linearized. The complete computational scheme is summarized in Algorithm 2, which includes consistent linearization of the nested iterative-subiterative scheme. In particular, once the implicit dependencies are correctly identified and introduced into the code, the consistent overall tangent (denoted as $\bar{\mathbb{L}}^{\text{alg}}$ in Algorithm 2) is obtained as the computational derivative $\hat{\delta}\bar{\boldsymbol{P}}/\hat{\delta}\bar{\boldsymbol{F}}$.

Algorithm 2 AD-based formulation of the incremental scheme for an elasto-plastic two-phase composite.

input: $\bar{\boldsymbol{F}}$, $\boldsymbol{c}^n$, $\mathbf{h}_1^n$, $\mathbf{h}_2^n$
$\boldsymbol{c} \leftarrow \boldsymbol{c}^n$
repeat
  $\boldsymbol{F}_1 \leftarrow \bar{\boldsymbol{F}} - \eta\boldsymbol{c}\otimes\boldsymbol{N}$
  $\boldsymbol{F}_2 \leftarrow \bar{\boldsymbol{F}} + (1-\eta)\boldsymbol{c}\otimes\boldsymbol{N}$
  $\{\mathbf{h}_1, \boldsymbol{P}_1, \mathbf{G}_1\} \leftarrow$ `StateUpdate` $\left[\boldsymbol{F}_1, \mathbf{h}_1^n\right]$
  $\{\mathbf{h}_2, \boldsymbol{P}_2, \mathbf{G}_2\} \leftarrow$ `StateUpdate` $\left[\boldsymbol{F}_2, \mathbf{h}_2^n\right]$
  $\mathbf{R} \leftarrow (\boldsymbol{P}_2 - \boldsymbol{P}_1)\boldsymbol{N}$
  $\mathbf{B} \leftarrow \dfrac{\hat{\delta}\mathbf{R}}{\hat{\delta}\boldsymbol{c}}$ ▷ tangent matrix, $\mathbf{B} = \dfrac{\partial\mathbf{R}}{\partial\boldsymbol{c}}$
  $\Delta\boldsymbol{c} \leftarrow -\mathbf{B}^{-1}\mathbf{R}$
  $\boldsymbol{c} \leftarrow \boldsymbol{c} + \Delta\boldsymbol{c}$
until $\|\Delta\boldsymbol{c}\| \le tol$
$\boldsymbol{c} \leftarrow \boldsymbol{c}\Big|_{\frac{\mathrm{D}\boldsymbol{c}}{\mathrm{D}\bar{\boldsymbol{F}}} = -\mathbf{B}^{-1}\frac{\hat{\delta}\mathbf{R}}{\hat{\delta}\bar{\boldsymbol{F}}}\Big|_{\boldsymbol{c}=\text{const}}}$
$\boldsymbol{F}_1 \leftarrow \bar{\boldsymbol{F}} - \eta\boldsymbol{c}\otimes\boldsymbol{N}$
$\boldsymbol{F}_2 \leftarrow \bar{\boldsymbol{F}} + (1-\eta)\boldsymbol{c}\otimes\boldsymbol{N}$
$\mathbf{h}_1 \leftarrow \mathbf{h}_1\Big|_{\frac{\mathrm{D}\mathbf{h}_1}{\mathrm{D}\boldsymbol{F}_1}=\mathbf{G}_1}$ ▷ introduce the implicit dependence of $\mathbf{h}_1$ on $\boldsymbol{F}_1$
$\mathbf{h}_2 \leftarrow \mathbf{h}_2\Big|_{\frac{\mathrm{D}\mathbf{h}_2}{\mathrm{D}\boldsymbol{F}_2}=\mathbf{G}_2}$ ▷ introduce the implicit dependence of $\mathbf{h}_2$ on $\boldsymbol{F}_2$
$\bar{W} \leftarrow (1-\eta)W_1(\boldsymbol{F}_1, \mathbf{h}_1) + \eta W_2(\boldsymbol{F}_2, \mathbf{h}_2)$
$\bar{\boldsymbol{P}} \leftarrow \left.\dfrac{\hat{\delta}\bar{W}}{\hat{\delta}\bar{\boldsymbol{F}}}\right|_{\boldsymbol{c}=\text{const}, \mathbf{h}_1=\text{const}, \mathbf{h}_2=\text{const}}$ ▷ AD exception ensures that $\bar{\boldsymbol{P}}$ is computed correctly
$\bar{\mathbb{L}}^{\text{alg}} \leftarrow \dfrac{\hat{\delta}\bar{\boldsymbol{P}}}{\hat{\delta}\bar{\boldsymbol{F}}}$
return: $\boldsymbol{c}$, $\bar{\boldsymbol{P}}$, $\bar{\mathbb{L}}^{\text{alg}}$, $\mathbf{h}_1$, $\mathbf{h}_2$

In practice, the iterative Newton scheme in Algorithm 2 is enhanced by a line search technique which significantly improves the robustness of the computational scheme. In fact, the robustness of the resulting scheme (convergence of the Newton method, maximum allowable time increment, etc.) does not differ from the respective performance of the classical (homogeneous) plasticity algorithms, see also [41,43] where a similar robustness is reported for the micromechanical Mori–Tanaka scheme developed for elasto-plastic and elasto-viscoplastic composites. The related details are omitted here.

References

[1] Belytschko T, Black T. Elastic crack growth in finite elements with minimal remeshing. Int J Numer Methods Eng 1999;45(5):601–20. https://doi.org/10.1002/(sici)1097-0207(19990620)45:5<601::aid-nme598>3.0.co;2-s.

[2] Moës N, Dolbow J, Belytschko T. A finite element method for crack growth without remeshing. Int J Numer Methods Eng 1999;46(1):131–50. https://doi.org/10.1002/(sici)1097-0207(19990910)46:1<131::aid-nme726>3.0.co;2-j.

[3] Burman E, Claus S, Hansbo P, Larson MG, Massing. CutFEM A. Discretizing geometry and partial differential equations. Int J Numer Methods Eng 2014;104(7):472–501. https://doi.org/10.1002/nme.4823.

[4] Song J-H, Areias PMA, Belytschko T. A method for dynamic crack and shear band propagation with phantom nodes. Int J Numer Methods Eng 2006;67(6):868–93. https://doi.org/10.1002/nme.1652.

[5] Sukumar N, Chopp D, Moës N, Belytschko T. Modeling holes and inclusions by level sets in the extended finite-element method. Comput Methods Appl Mech Eng 2001;190(46–47):6183–200. https://doi.org/10.1016/s0045-7825(01)00215-8.

[6] Belytschko T, Parimi C, Moës N, Sukumar N, Usui S. Structured extended finite element methods for solids defined by implicit surfaces. Int J Numer Methods Eng 2002;56(4):609–35. https://doi.org/10.1002/nme.686.

[7] Moës N, Cloirec M, Cartraud P, Remacle J-F. A computational approach to handle complex microstructure geometries. Comput Methods Appl Mech Eng 2003;192(28–30):3163–77. https://doi.org/10.1016/s0045-7825(03)00346-3.

[8] Hughes T, Cottrell J, Bazilevs Y. Isogeometric analysis: CAD, finite elements, NURBS, exact geometry and mesh refinement. Comput Methods Appl Mech Eng 2005;194(39–41):4135–95. https://doi.org/10.1016/j.cma.2004.10.008.
[9] Luycker ED, Benson DJ, Belytschko T, Bazilevs Y, Hsu MC. X-FEM in isogeometric analysis for linear fracture mechanics. Int J Numer Methods Eng 2011;87(6):541–65. https://doi.org/10.1002/nme.3121.
[10] Ghorashi SS, Valizadeh N, Mohammadi S. Extended isogeometric analysis for simulation of stationary and propagating cracks. Int J Numer Methods Eng 2011;89(9):1069–101. https://doi.org/10.1002/nme.3277.
[11] Tambat A, Subbarayan G. Isogeometric enriched field approximations. Comput Methods Appl Mech Eng 2012;245–246:1–21. https://doi.org/10.1016/j.cma.2012.06.006.
[12] Noël L, Schmidt M, Doble K, Evans JA, Maute K. XIGA: an eXtended IsoGeometric analysis approach for multi-material problems. Comput Mech 2022;70(6):1281–308. https://doi.org/10.1007/s00466-022-02200-y.
[13] Osher S, Sethian JA. Fronts propagating with curvature-dependent speed: algorithms based on Hamilton–Jacobi formulations. J Comput Phys 1988;79(1):12–49. https://doi.org/10.1016/0021-9991(88)90002-2.
[14] Li Z, Yang X. An immersed finite element method for elasticity equations with interfaces. Contemp Math 2005;383:285–98.
[15] Lin T, Zhang X. Linear and bilinear immersed finite elements for planar elasticity interface problems. J Comput Appl Math 2012;236(18):4681–99. https://doi.org/10.1016/j.cam.2012.03.012.
[16] Liu W, Yang Q, Mohammadizadeh S, Su X. An efficient augmented finite element method for arbitrary cracking and crack interaction in solids. Int J Numer Methods Eng 2014;99(6):438–68. https://doi.org/10.1002/nme.4697.
[17] Essongue S, Couégnat G, Martin E. Performance assessment of the augmented finite element method for the modeling of weak discontinuities. Int J Numer Methods Eng 2020;122(1):172–89. https://doi.org/10.1002/nme.6530.
[18] Li Z, Lin T, Wu X. New Cartesian grid methods for interface problems using the finite element formulation. Numer Math 2003;96(1):61–98. https://doi.org/10.1007/s00211-003-0473-x.
[19] Li K, Atallah NM, Main GA, Scovazzi G. The shifted interface method: a flexible approach to embedded interface computations. Int J Numer Methods Eng 2019;121(3):492–518. https://doi.org/10.1002/nme.6231.
[20] Li K. The shifted interface/boundary method for embedded domain computations. PhD thesis. Duke University; 2021.
[21] Moulinec H, Suquet P. A numerical method for computing the overall response of nonlinear composites with complex microstructure. Comput Methods Appl Mech Eng 1998;157(1–2):69–94. https://doi.org/10.1016/s0045-7825(97)00218-1.
[22] Brisard S, Dormieux L. FFT-based methods for the mechanics of composites: a general variational framework. Comput Mater Sci 2010;49(3):663–71. https://doi.org/10.1016/j.commatsci.2010.06.009.
[23] Toulemonde C, Masson R, Gharib JE. Modeling the effective elastic behavior of composites: a mixed finite element and homogenisation approach. C R, Méc 2008;336(3):275–82. https://doi.org/10.1016/j.crme.2007.11.024.
[24] Gélébart L, Ouaki F. Filtering material properties to improve FFT-based methods for numerical homogenization. J Comput Phys 2015;294:90–5. https://doi.org/10.1016/j.jcp.2015.03.048.
[25] Kabel M, Merkert D, Schneider M. Use of composite voxels in FFT-based homogenization. Comput Methods Appl Mech Eng 2015;294:168–88. https://doi.org/10.1016/j.cma.2015.06.003.
[26] Mareau C, Robert C. Different composite voxel methods for the numerical homogenization of heterogeneous inelastic materials with FFT-based techniques. Mech Mater 2017;105:157–65. https://doi.org/10.1016/j.mechmat.2016.12.002.
[27] Kabel M, Fink A, Schneider M. The composite voxel technique for inelastic problems. Comput Methods Appl Mech Eng 2017;322:396–418. https://doi.org/10.1016/j.cma.2017.04.025.
[28] Kabel M, Ospald F, Schneider M. A model order reduction method for computational homogenization at finite strains on regular grids using hyperelastic laminates to approximate interfaces. Comput Methods Appl Mech Eng 2016;309:476–96. https://doi.org/10.1016/j.cma.2016.06.021.
[29] Keshav S, Fritzen F, Kabel M. FFT-based homogenization at finite strains using composite boxels (ComBo). Comput Mech 2022. https://doi.org/10.1007/s00466-022-02232-4.
[30] Šilhavý M. The mechanics and thermodynamics of continuous media. Springer Berlin Heidelberg; 1997.
[31] Stupkiewicz S. Micromechanics of contact and interphase layers. Springer Berlin Heidelberg; 2007.
[32] Keyak J, Meagher J, Skinner H, Mote C. Automated three-dimensional finite element modelling of bone: a new method. J Biomed Eng 1990;12(5):389–97. https://doi.org/10.1016/0141-5425(90)90022-f.
[33] Terada K, Miura T, Kikuchi N. Digital image-based modeling applied to the homogenization analysis of composite materials. Comput Mech 1997;20(4):331–46. https://doi.org/10.1007/s004660050255.
[34] Lian WD, Legrain G, Cartraud P. Image-based computational homogenization and localization: comparison between X-FEM/levelset and voxel-based approaches. Comput Mech 2012;51(3):279–93. https://doi.org/10.1007/s00466-012-0723-9.
[35] Parvizian J, Düster A, Rank E. Finite cell method. Comput Mech 2007;41(1):121–33. https://doi.org/10.1007/s00466-007-0173-y.
[36] Korelc J. Automation of primal and sensitivity analysis of transient coupled problems. Comput Mech 2009;44(5):631–49. https://doi.org/10.1007/s00466-009-0395-2.
[37] Korelc J, Wriggers P. Automation of finite element methods. Springer International Publishing; 2016.
[38] de Souza Neto E, Perić D, Dutko M, Owen D. Design of simple low order finite elements for large strain analysis of nearly incompressible solids. Int J Solids Struct 1996;33(20–22):3277–96. https://doi.org/10.1016/0020-7683(95)00259-6.
[39] Simo JC, Hughes TJR. Computational inelasticity. Springer-Verlag; 1998.
[40] Korelc J, Stupkiewicz S. Closed-form matrix exponential and its application in finite-strain plasticity. Int J Numer Methods Eng 2014;98(13):960–87. https://doi.org/10.1002/nme.4653.
[41] Sadowski P, Kowalczyk-Gajewska K, Stupkiewicz S. Consistent treatment and automation of the incremental Mori–Tanaka scheme for elasto-plastic composites. Comput Mech 2017;60(3):493–511. https://doi.org/10.1007/s00466-017-1418-z.
[42] Michaleris P, Tortorelli DA, Vidal CA. Tangent operators and design sensitivity formulations for transient non-linear coupled problems with applications to elastoplasticity. Int J Numer Methods Eng 1994;37(14):2471–99. https://doi.org/10.1002/nme.1620371408.
[43] Sadowski P, Kowalczyk-Gajewska K, Stupkiewicz S. Spurious softening in the macroscopic response predicted by the additive tangent Mori–Tanaka scheme for elastic–viscoplastic composites. Eur J Mech A, Solids 2021;90:104339. https://doi.org/10.1016/j.euromechsol.2021.104339.